



## LJMU Research Online

Wang, B, Leja, J, Labbé, I, Bezanson, R, Whitaker, KE, Brammer, G, Furtak, LJ, Weaver, JR, Price, SH, Zitrin, A, Atek, H, Coe, D, Cutler, SE, Dayal, P, van Dokkum, P, Feldmann, R, Marchesini, D, Franx, M, Förster Schreiber, N, Fujimoto, S, Geha, M, Glazebrook, K, de Graaff, A, Greene, JE, Juneau, S, Kassin, S, Kriek, M, Khullar, G, Maseda, M, Mowla, LA, Muzzin, A, Nanayakkara, T, Nelson, EJ, Oesch, PA, Pacifici, C, Pan, R, Papovich, C, Setton, DJ, Shapley, AE, Smit, R, Stefanon, M, Suess, KA, Taylor, EN and Williams, CC

**The UNCOVER Survey: A First-look HST+JWST Catalog of Galaxy Redshifts and Stellar Population Properties Spanning  $0.2 \lesssim z \lesssim 15$**

<http://researchonline.ljmu.ac.uk/id/eprint/23997/>

### Article

**Citation** (please note it is advisable to refer to the publisher's version if you intend to cite from this work)

**Wang, B, Leja, J, Labbé, I, Bezanson, R, Whitaker, KE, Brammer, G, Furtak, LJ, Weaver, JR, Price, SH, Zitrin, A, Atek, H, Coe, D, Cutler, SE, Dayal, P, van Dokkum, P, Feldmann, R, Marchesini, D, Franx, M, Förster Schreiber, N, Fuiimoto. S. Geha. M. Glazebrook. K. de Graaff. A. Greene. JE. Juneau. S.**

LJMU has developed [LJMU Research Online](#) for users to access the research output of the University more effectively. Copyright © and Moral Rights for the papers on this site are retained by the individual authors and/or other copyright owners. Users may download and/or print one copy of any article(s) in LJMU Research Online to facilitate their private study or for non-commercial research. You may not engage in further distribution of the material or use it for any profit-making activities or any commercial gain.

The version presented here may differ from the published version or from the version of the record. Please see the repository URL above for details on accessing the published version and note that access may require a subscription.










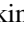



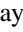


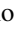
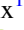

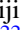
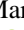




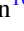


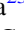

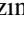
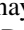
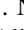
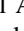
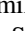
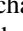



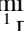
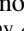
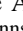
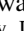
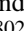
<http://researchonline.ljmu.ac.uk/>

For more information please contact [researchonline@ljmu.ac.uk](mailto:researchonline@ljmu.ac.uk)

<http://researchonline.ljmu.ac.uk/>



# The UNCOVER Survey: A First-look HST+JWST Catalog of Galaxy Redshifts and Stellar Population Properties Spanning $0.2 \lesssim z \lesssim 15$

Bingjie Wang (王冰洁)<sup>1,2,3</sup> , Joel Leja<sup>1,2,3</sup> , Ivo Labbé<sup>4</sup> , Rachel Bezanson<sup>5</sup> , Katherine E. Whitaker<sup>6,7</sup> , Gabriel Brammer<sup>7</sup> , Lukas J. Furtak<sup>8</sup> , John R. Weaver<sup>6</sup> , Sedona H. Price<sup>5</sup> , Adi Zitrin<sup>8</sup> , Hakim Atek<sup>9</sup> , Dan Coe<sup>10,11,12</sup> , Sam E. Cutler<sup>6</sup> , Pratika Dayal<sup>13</sup> , Pieter van Dokkum<sup>14</sup> , Robert Feldmann<sup>15</sup> , Danilo Marchesini<sup>16</sup> , Marijn Franx<sup>17</sup> , Natascha Förster Schreiber<sup>18</sup> , Seiji Fujimoto<sup>19,37</sup> , Marla Geha<sup>14</sup> , Karl Glazebrook<sup>4</sup> , Anna de Graaff<sup>20</sup> , Jenny E. Greene<sup>21</sup> , Stéphanie Juneau<sup>22</sup> , Susan Kassin<sup>10</sup> , Mariska Kriek<sup>17</sup> , Gourav Khullar<sup>5</sup> , Michael Maseda<sup>23</sup> , Lamiya A. Mowla<sup>24</sup> , Adam Muzzin<sup>25</sup> , Themiya Nanayakkara<sup>4</sup> , Erica J. Nelson<sup>26</sup> , Pascal A. Oesch<sup>7,27</sup> , Camilla Pacifici<sup>10</sup> , Richard Pan<sup>16</sup> , Casey Papovich<sup>28,29</sup> , David J. Setton<sup>5</sup> , Alice E. Shapley<sup>30</sup> , Renske Smit<sup>31</sup> , Mauro Stefanon<sup>32,33</sup> , Katherine A. Suess<sup>34,37</sup> , Edward N. Taylor<sup>4</sup> , and Christina C. Williams<sup>35,36</sup> 

<sup>1</sup> Department of Astronomy & Astrophysics, The Pennsylvania State University, University Park, PA 16802, USA; [bwang@psu.edu](mailto:bwang@psu.edu)

<sup>2</sup> Institute for Computational & Data Sciences, The Pennsylvania State University, University Park, PA 16802, USA

<sup>3</sup> Institute for Gravitation and the Cosmos, The Pennsylvania State University, University Park, PA 16802, USA

<sup>4</sup> Centre for Astrophysics and Supercomputing, Swinburne University of Technology, Melbourne, VIC 3122, Australia

<sup>5</sup> Department of Physics & Astronomy and PITT PACC, University of Pittsburgh, Pittsburgh, PA 15260, USA

<sup>6</sup> Department of Astronomy, University of Massachusetts, Amherst, MA 01003, USA

<sup>7</sup> Cosmic Dawn Center (DAWN), Niels Bohr Institute, University of Copenhagen, Jagtvej 128, København N DK-2200, Denmark

<sup>8</sup> Department of Physics, Ben-Gurion University of the Negev, P.O. Box 653, Beer-Sheva 8410501, Israel

<sup>9</sup> Institut d'Astrophysique de Paris, CNRS, Sorbonne Université, 98 bis Boulevard Arago, F-75014, Paris, France

<sup>10</sup> Space Telescope Science Institute, Baltimore, MD 21218, USA

<sup>11</sup> Association of Universities for Research in Astronomy, Inc. for the European Space Agency, USA

<sup>12</sup> Center for Astrophysical Sciences, Department of Physics & Astronomy, Johns Hopkins University, Baltimore, MD 21218, USA

<sup>13</sup> Kapteyn Astronomical Institute, University of Groningen, P.O. Box 800, 9700 AV Groningen, The Netherlands

<sup>14</sup> Department of Astronomy, Yale University, New Haven, CT 06511, USA

<sup>15</sup> Institute for Computational Science, University of Zurich, Winterthurerstrasse 190, CH-8006 Zurich, Switzerland

<sup>16</sup> Department of Physics & Astronomy, Tufts University, Medford, MA 02155, USA

<sup>17</sup> Leiden Observatory, Leiden University, P.O.Box 9513, NL-2300 AA Leiden, The Netherlands

<sup>18</sup> Max-Planck-Institut für extraterrestrische Physik, Gießenbachstraße 1, D-85748 Garching, Germany

<sup>19</sup> Department of Astronomy, The University of Texas at Austin, Austin, TX 78712, USA

<sup>20</sup> Max-Planck-Institut für Astronomie, Königstuhl 17, D-69117, Heidelberg, Germany

<sup>21</sup> Department of Astrophysical Sciences, Princeton University, Princeton, NJ 08544, USA

<sup>22</sup> NSF's National Optical-Infrared Astronomy Research Laboratory, 950 N. Cherry Avenue, Tucson, AZ 85719, USA

<sup>23</sup> Department of Astronomy, University of Wisconsin-Madison, Madison, WI 53706, USA

<sup>24</sup> Dunlap Institute for Astronomy & Astrophysics, Toronto, Ontario M5S 3H4, Canada

<sup>25</sup> Department of Physics & Astronomy, York University, Toronto, Ontario ON M3J 1P3, Canada

<sup>26</sup> Department for Astrophysical & Planetary Science, University of Colorado, Boulder, CO 80309, USA

<sup>27</sup> Department of Astronomy, University of Geneva, Chemin Pegasi 51, 1290 Versoix, Switzerland

<sup>28</sup> Department of Physics & Astronomy, Texas A&M University, College Station, TX 77843-4242, USA

<sup>29</sup> George P. and Cynthia Woods Mitchell Institute for Fundamental Physics and Astronomy, Texas A&M University, College Station, TX 77843-4242, USA

<sup>30</sup> Department of Physics & Astronomy, University of California: Los Angeles, Los Angeles, CA 90095, USA

<sup>31</sup> Astrophysics Research Institute, Liverpool John Moores University, 146 Brownlow Hill, Liverpool L3 5RF, UK

<sup>32</sup> Departament d'Astronomia i Astrofísica, Universitat de València, C. Dr. Moliner 50, E-46100 Burjassot, Valencia, Spain

<sup>33</sup> Unidad Asociada CSIC "Grupo de Astrofísica Extragaláctica y Cosmología" (Instituto de Física de Cantabria—Universitat de València), Spain

<sup>34</sup> Kavli Institute for Particle Astrophysics and Cosmology and Department of Physics, Stanford University, Stanford, CA 94305, USA

<sup>35</sup> NSF's National Optical-Infrared Astronomy Research Laboratory, Tucson, AZ 85719, USA

<sup>36</sup> Steward Observatory, University of Arizona, Tucson, AZ 85721, USA

Received 2023 May 15; revised 2023 September 6; accepted 2023 October 2; published 2023 December 28

## Abstract

The recent UNCOVER survey with the James Webb Space Telescope (JWST) exploits the nearby cluster A2744 to create the deepest view of our Universe to date by leveraging strong gravitational lensing. In this work, we perform photometric fitting of more than 50,000 robustly detected sources out to  $z \sim 15$ . We show the redshift evolution of stellar ages, star formation rates, and rest-frame colors across the full range of  $0.2 \lesssim z \lesssim 15$ . The galaxy properties are inferred using the *Prospector* Bayesian inference framework using informative *Prospector*- $\beta$  priors on the masses and star formation histories to produce joint redshift and stellar populations posteriors. Additionally, lensing magnification is performed on the fly to ensure consistency with the scale-dependent priors. We show that this approach produces excellent photometric redshifts with  $\sigma_{\text{NMAD}} \sim 0.03$ , of a similar quality to the established photometric redshift code *EAzY*. In line with the open-source scientific objective of this Treasury survey, we

<sup>37</sup> Hubble Fellow.



publicly release the stellar population catalog with this paper, derived from our photometric catalog adapting aperture sizes based on source profiles. This release (the catalog and all related documentation are accessible via the UNCOVER survey web page: <https://jwst-uncover.github.io/DR2.html#SPSCatalogs> with a copy deposited to Zenodo at doi:10.5281/zenodo.8401181) includes posterior moments, maximum likelihood spectra, star formation histories, and full posterior distributions, offering a rich data set to explore the processes governing galaxy formation and evolution over a parameter space now accessible by JWST.

*Unified Astronomy Thesaurus concepts:* [Abell clusters \(9\)](#); [Catalogs \(205\)](#); [Galaxy evolution \(594\)](#); [James Webb Space Telescope \(2291\)](#); [Hubble Space Telescope \(761\)](#); [Spectral energy distribution \(2129\)](#)

## 1. Introduction

The Hubble Space Telescope (HST) has secured a lasting legacy in mapping the key epochs of galaxy assembly via Treasury programs (e.g., Grogin et al. 2011; Brammer et al. 2012). JWST, with its sensitive NIRC*am* imaging and NIRS*pec* spectroscopy at 1–5  $\mu\text{m}$  (Böker et al. 2023; Rieke et al. 2023; Rigby et al. 2023), promises to not only extend this legacy, but also reveal new mysteries of the distant Universe out to  $z \sim 15$  and beyond. Thus far, data from the JWST Early Release Science programs have already shed new light on the early phases of galactic evolution (e.g., Treu et al. 2022; Finkelstein et al. 2023). The JWST extragalactic Treasury survey, Ultradeep NIRS*pec* and NIRC*am* ObserVations before the Epoch of Reionization (UNCOVER; Bezanson et al. 2022), has completed its primary NIRC*am* imaging observations on and around the gravitational lensing cluster A2744 at  $z = 0.308$  in 2022 November. The images reach depths of  $\sim 30$  AB magnitudes. After accounting for gravitational lensing, the intrinsic depths reach  $\gtrsim 31$ – $32$  AB magnitudes, making UNCOVER the deepest survey in Cycle 1 of JWST observations. The quest for a coherent understanding of the Universe in the newly observed parameter space is just beginning.

For the first time, it is possible to observe galaxies and candidates spanning  $0.2 \lesssim z \lesssim 15$  and infer their stellar population properties. In the context of UNCOVER, spectroscopically confirmed galaxies at  $z > 12$  and an X-ray luminous supermassive black hole at  $z = 10.1$  are studied in detail in Wang et al. (2023a) and Goulding et al. (2023), respectively, whereas a systematic search for  $z_{\text{spec}} \gtrsim 9$  sources is carried out in Fujimoto et al. (2023b). The core of this paper is to present a galaxy catalog containing key stellar population metrics over the full dynamic range probed by the survey. This work is part of the second data release (DR2) from UNCOVER. In accordance with the open-data intent of the Treasury survey, we have made publicly available the imaging mosaics (Bezanson et al. 2022), updated strong lensing model (Furtak et al. 2023), and first-look photometric catalogs (Weaver et al. 2024). This paper constitutes the final installation of UNCOVER DR2: inferred galaxy properties, including redshifts, stellar masses, metallicities, ages, star formation rates (SFRs), dust attenuation values, and fractional mid-infrared active galactic nucleus (AGN) luminosities. It is accompanied by the magnification factor, and additionally the radial magnification, tangential magnification, and shear, consistent with the inferred redshifts. The full posterior distributions are also released.

The main data products in this work are inferred using the *Prospector* Bayesian framework (Johnson et al. 2021), with two notable modifications. First, we optimize our priors for recovering accurate photometric redshifts by including observationally motivated, joint priors on stellar mass, stellar

metallicity, and star formation history (SFH) from *Prospector- $\beta$*  (Wang et al. 2023c). Second, we solve the magnification–redshift relationship on the fly within *Prospector* to take advantage of the mass-dependent priors, in contrast to the traditional approach where physical parameters are scaled by magnification factors postfit.

Inferring redshifts across a wide range of distances and galaxy properties based solely on photometric data push the stellar populations models into new, exciting, and largely uncalibrated regimes. Comparisons between different photo- $z$  codes have clearly highlighted that accuracy in this space depends strongly on the assumptions that go into the code (e.g., Kodra et al. 2023). Given the novelty of our *Prospector* model, we cross-check our redshifts with those from the established template-fitting code *EAzY* (Brammer et al. 2008). We additionally analyze the effect of varying template sets within *EAzY* by comparing results from the default set *fsp*s to *sfhz*. The latter incorporates redshift-dependent SFHs and a realistic emission-line model at  $z \sim 8$  (Carnall et al. 2023).

The structure of this paper is as follows. Section 2 summarizes the photometric data. Section 3 details the spectral energy distribution (SED) modeling. Section 4 presents the inferred parameters. Section 5 discusses known problems in the photometry and in the modeling, and how these may affect the accuracy of the inferred stellar populations parameters. Section 6 concludes with a brief summary and the format of our catalogs.

Where applicable, we adopt the best-fit cosmological parameters from the 9 yr results from the Wilkinson Microwave Anisotropy Probe mission:  $H_0 = 69.32 \text{ km s}^{-1} \text{ Mpc}^{-1}$ ,  $\Omega_M = 0.2865$ , and  $\Omega_\Lambda = 0.7135$  (Hinshaw et al. 2013), and a Chabrier initial mass function (IMF; Chabrier 2003). Unless otherwise mentioned, we report the median of the posterior, and  $1\sigma$  error bars are the 16th and 84th percentiles.

## 2. Data

The photometry includes all public JWST/NIRC*am*, HST/Advanced Camera for Surveys (ACS) and HST/WFC3 imaging of A2744 available to date. Specifically, the JWST data include the Cycle 1 Treasury program UNCOVER covering  $\sim 45 \text{ arcmin}^2$  (PIs: Labbé & Bezanson, JWST-GO-2561; Bezanson et al. 2022), the Early Release Science program Grism Lens Amplified Survey from Space (GLASS; PI: Treu, JWST-ERS-1324; Treu et al. 2022), and a Director’s Discretionary program (JWST-DD-2756, PI: Chen). These observations span  $\sim 1$ – $5 \mu\text{m}$  in the observer frame in eight filters: F090W, F115W, F150W, F200W, F277W, F356W, F410M, and F444W. The HST data, taken from the public archive, consist of HST-GO-11689 (PI: Dupke), HST-GO-13386 (PI: Rodney), HST-DD-13495 (PI: Lotz; Lotz et al. 2017), and HST-GO-15117 (PI: Steinhardt; Steinhardt et al. 2020). These additional observations span  $\sim 0.4$ – $1.6 \mu\text{m}$  in the

observer frame in seven filters: F435W, F606W, F814W, F105W, F125W, F140W, and F160W. Details of these programs including imaging depths and ancillary information are summarized in Tables 1 and 3 in Bezanson et al. (2022). A small subsample has detections or upper limits from the Deep UNCOVER–Atacama Large Millimeter/submillimeter Array (ALMA) Legacy High-Z (DUALZ) Survey (Fujimoto et al. 2023a). The transmission curve of this ALMA band is approximated as a top-hat function spanning 1249.9–1351.0  $\mu\text{m}$ .

As part of UNCOVER DR2, we have released F277W + F356W + F444W–selected photometric catalogs containing total fluxes for 61,648 sources (Weaver et al. 2024). In this work we fit galaxy SEDs to the “supercatalog,” which uses adaptive aperture selection based on their isophotal areas following Labbé et al. (2003). We share publicly the inferred parameters for the full sample. However, it is worth noting that a subsample of 55,613 objects is deemed to have reliable photometry, i.e., `use_phot = 1` in the photometric catalog. Furthermore, 15,861 objects in this subsample are flagged as possible blends (`flag_kron = 1`), and therefore their photometry is not corrected to total based on a kron ellipse but instead is corrected assuming a point-like morphology. Photometry performed on simulated galaxies with realistic sizes indicate that the total photometry of these objects may be underestimated by a factor of 2 in  $0''.32$ – $0''.70$  apertures, with larger  $1''.00$ – $1''.40$  apertures miss  $<10\%$  of the total flux. Consequently, the physical parameters derived in this work including stellar mass and rest-frame fluxes are liable to be underestimated. Details on the selection criteria for the `use_phot` and `flag_kron` flags are presented in Section 4.6 in Weaver et al. (2024).

A total of  $\sim 400$  reliable, unblended sources in the UNCOVER photometric catalogs have spectroscopic redshifts collected from the NASA/Infrared Processing and Analysis Center Extragalactic Database, and from the literature. The latter consists of measurements taken with HST as part of GLASS (Treu et al. 2015), and with the Multi Unit Spectroscopic Explorer (Richard et al. 2021). We utilize this sample to evaluate the accuracy of our photometric redshift recovery.

### 3. SED Fitting

This section describes the core of this work—inferring physical parameters of the galaxy populations from the photometry. An overview of the inferred parameters of our catalog is shown in Figure 1.

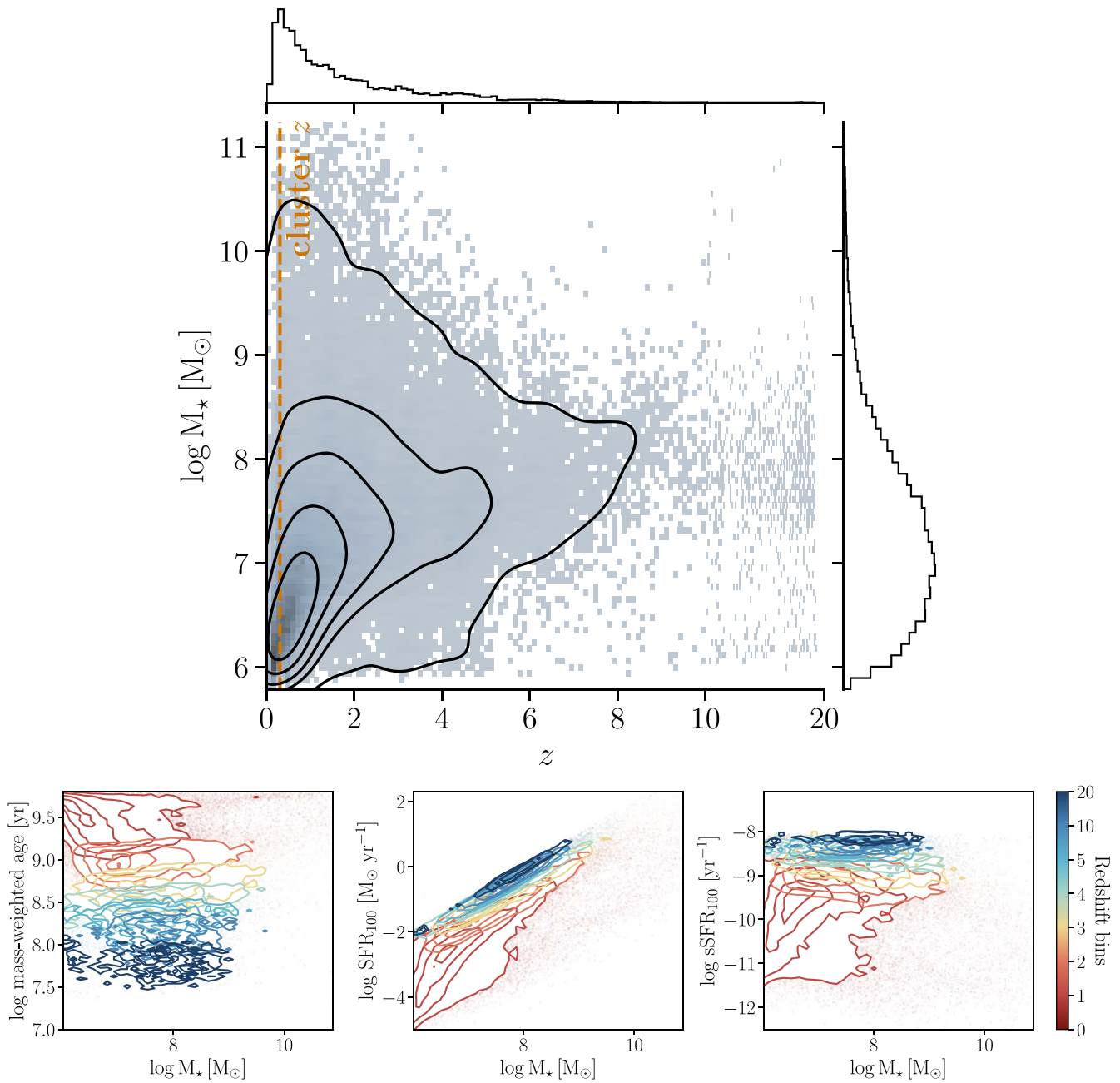
In what follows, we first describe our modified `Prospector` model, which includes physically motivated priors to produce joint constraints of redshifts, stellar masses, and other key stellar populations metrics optimally across any redshift range, and a consistent treatment of lensing magnification during model fitting. We then outline the adopted `EAzY` settings, and its two template sets, `fsps` and `sfhz`. A minimum error floor of 5% is imposed in all fits to reflect the additional systematic uncertainties—the calibration uncertainties of JWST/NIRCam at this early stage (Boyer et al. 2022), as well as uncertainties in the stellar population synthesis (SPS).

#### 3.1. Prospector

The main data products in the catalog are inferred using the `Prospector` Bayesian inference framework (Johnson et al. 2021). The building blocks of these fits, i.e., the simple stellar populations (SSPs), come from `FSPS` (Conroy & Gunn 2010), where we adopt `MIST` isochrones (Choi et al. 2016; Dotter 2016) and the `MILES` stellar library (Sánchez-Blázquez et al. 2006). The composite stellar populations (CSPs) are modeled with `Prospector- $\beta$`  (Wang et al. 2023c), which follows `Prospector- $\alpha$`  (Leja et al. 2017) in many components. In this section, we begin with the common elements in `Prospector- $\alpha$` , and then proceed to the new additions from `Prospector- $\beta$` , namely the joint priors on stellar mass, stellar metallicity, and SFH. We end with a novel modification in the likelihood calculation which allows for a self-consistent treatment for lensing magnification during model fitting.

The SFH is modeled as mass formed in seven logarithmically spaced time bins, and assumes a continuity prior to ensure smooth transitions between bins (Leja et al. 2019a). The scheme for the age bins is refined in this work. For  $z < 3$ , we keep the conventional definition in which the first two bins are always 30 Myr and 100 Myr respectively, whereas for  $z \geq 3$ , we only require that the first bin is always 13.47 Myr. In both cases, the last bin is 10% of the age of the Universe at a given redshift, and the intervening bins are evenly spaced in logarithmic time. This new scheme ensures that no age bins are overly wide in the early Universe. Nebular emission is included using a precomputed `Cloudy` grid (Byler et al. 2017). Dust is described using a two-component model (Charlot & Fall 2000) with a flexible dust attenuation curve (Noll et al. 2009). We also fit for the stellar metallicity, and the normalization and dust optical depth of mid-infrared AGNs. Dust emission is included in all fits (Draine & Li 2007), with the mass fraction of polycyclic aromatic hydrocarbons (PAHs) left free. Attenuation by the intergalactic medium (IGM) is assumed to follow Madau (1995).

In contrast to previous large-scale applications of `Prospector` to broadband photometry, which typically fix the redshift to a value determined by an external photo- $z$  code (e.g., Leja et al. 2019b), here we fit directly for redshift and use informed priors for the stellar mass, stellar metallicity, and SFH in the `Prospector- $\beta$`  model. We opt for this approach to take the full advantage of the `Prospector` Bayesian inference framework, and thus to obtain consistent joint constraints on the probability distribution of the full posterior. Following Wang et al. (2023c), we first include a mass prior  $P(\log M^*|z)$ , constructed from the observed mass functions between  $0.2 < z < 3$  (Leja et al. 2020). For  $z < 0.2$  and  $z > 3$ , we take the nearest-neighbor solution, i.e., the  $z = 0.2$  and  $z = 3$  mass functions. This applies the mass function as a prior where it is well measured, and avoids relying on simulation predictions while making a reasonable null hypothesis in the absence of observational constraints. Second, we use a dynamic SFH prior, meaning that the shape of the SFH is dependent on redshift and stellar mass. The expectation value of this prior is matched to the cosmic SFR density (Behroozi et al. 2019); in other words, it encourages rising histories early in the Universe, and falling histories late in the Universe. This prior additionally reflects the consistent observational finding that massive galaxies form much earlier than low-mass galaxies (Cowie et al. 1996; Thomas et al. 2005) by introducing a hyperparameter that scales the expectation value for the shape of SFH



**Figure 1.** An overview of the key inferred parameters in our catalog. Upper panel: joint distribution of redshifts and stellar masses. The  $x$ -axis is in linear scale at  $z \leq 10$ , while in logarithmic scale at  $z > 10$ . The redshift at which the A2744 cluster resides ( $z = 0.308$ ) is indicated by an orange dashed line. The secondary peak in the mass distribution at  $\sim 10^6 M_\odot$  is mainly due to the large population of globular clusters. Lower panel: mass-weighted ages, SFRs (100 Myr), and specific star formation rates (sSFRs; 100 Myr) as functions of stellar masses in redshift bins.

with mass, such that massive galaxies have more falling SFHs and low-mass galaxies have more rising SFHs. As noted in Wang et al. (2023c), even though the high-redshift constraints on galaxy evolution remain uncertain, these priors still represent a better expectation than the null expectation of uniform priors. Third, we place a prior based on the stellar mass–stellar metallicity relationship measured from the Sloan Digital Sky Survey (Gallazzi et al. 2005). Following Leja et al. (2019a), we take the conservative approach of widening the confidence intervals from this relationship by a factor of 2 to account for potential unknown systematics or redshift evolution. This prior neglects predictions from galaxy formation

models, which suggest a smaller scatter and a relatively strong redshift evolution (Ma et al. 2016; Feldmann et al. 2023).

A complete list of the free parameters and their associated priors is summarized in Table 1. Only the first eight parameters in the table are used to infer the physical parameters that are provided in the first public release. The other parameters are used as nuisance parameters in the great majority of cases, and will be examined further in the future.

It is worth noting that we correct for lensing magnification simultaneously while fitting the full set of parameters. Gravitational lensing is in general achromatic (i.e., the deflection angle of a light ray is independent of its wavelength), meaning that colors are conserved. Therefore, while the

**Table 1**  
Prospector- $\beta$  Parameters and Priors Adopted in This Paper

Parameter	Description	Prior
$z$	redshift	uniform: min = 0, max = 20
$\log (M/M_{\odot})$	total stellar mass formed	mass functions in Leja et al. (2020), as implemented in Wang et al. (2023c)
SFH	ratio of SFRs in adjacent log-spaced time bins	SFH ( $M, z$ ) (Wang et al. 2023c)
$\log (Z^*/Z_{\odot})$	stellar metallicity	Gaussian approximating the $M-Z^*$ relationship of Gallazzi et al. (2005)
$n$	power-law index for a Calzetti et al. (2000) attenuation curve	uniform: min = -1.0, max = 0.4
$\hat{\tau}_{\text{dust},2}$	optical depth of diffuse dust (Charlot & Fall 2000)	truncated normal: min = 0, max = 4, $\mu = 0.3$ , $\sigma = 1$
$\hat{\tau}_{\text{dust},1}/\hat{\tau}_{\text{dust},2}$	ratio between the optical depths of birth cloud dust and diffuse dust (Charlot & Fall 2000)	truncated normal: min = 0, max = 2, $\mu = 1$ , $\sigma = 0.3$
$\log f_{\text{AGN}}$	ratio between the object's AGN luminosity and its bolometric luminosity	uniform: min = -5, max = log 3
$\log \tau_{\text{AGN}}$	optical depth of the AGN torus dust	uniform: min = log 5, max = log 150
$\log (Z_{\text{gas}}/Z_{\odot})$	gas-phase metallicity	uniform: min = -2.0, max = 0.5
$q_{\text{PAH}}$	fraction of grain mass in PAHs (Draine & Li 2007)	truncated normal: min = 0, max = 7, $\mu = 2$ , $\sigma = 2$

magnification factor,  $\mu$ , depends on redshift and source position, it is not conventionally accounted for in the process of SED fitting. Rather, the modeled fluxes and the scale-dependent physical parameters such as stellar mass are often divided by  $\mu$  postfit, or the observed fluxes are demagnified before fitting using external redshift information. However, scale-dependent priors in Prospector- $\beta$  necessitate a self-consistent treatment of  $\mu$ . We devise a simple method: given a source position, we read in the convergence,  $\kappa$ , and shear,  $\gamma$ , from the  $0''.1 \text{ pixel}^{-1}$  resolution maps provided as part of UNCOVER DR2 (Furtak et al. 2023).<sup>38</sup> These maps are normalized such that  $D_{ds}/D_d = 1$ , where  $D_{ds}$  is the angular diameter distance between the lens and the source planes, and  $D_d$  is the distance between the lens plane and the observer. Then in each draw of the redshift during sampling, we multiply  $\kappa$  and  $\gamma$  by the  $D_{ds}/D_d$  of the source, and magnify the model photometry by  $\mu$ , which is calculated as

$$\mu = \frac{1}{|(1 - \kappa^2) - \gamma^2|}. \quad (1)$$

Critically, magnifying the model fluxes and demagnifying the observations are not equivalent due to the definition of likelihood in Prospector

$$\ln \mathcal{L} = \sum_{n=1}^N \ln \left[ \frac{1}{\sqrt{2\pi\sigma^2}} \cdot \exp\left(\frac{(x_n - \alpha)^2}{-2\sigma^2}\right) \right], \quad (2)$$

where  $\sigma$  is the observed uncertainties,  $x_n$  is the observed flux in the  $n$ th photometric band, and  $\alpha$  is the model uncertainties. The often neglected prefactor is properly included here because Prospector offers the functionality of estimating the observational uncertainties simultaneously with the object parameters. In the context of the magnification calculation, if we change the observational uncertainties with redshift, the prefactor works to minimize these uncertainties, or in other words to maximize  $\mu$ . Therefore, we must magnify the model fluxes for the likelihood to behavior correctly.

The posterior space is sampled with the nested sampler dynesty (Speagle 2020), and a neural net emulator, dubbed parrot, which mimics SPS models, is used to decrease the

runtime (Alsing et al. 2020; Mathews et al. 2023). Given that this work is the first large-scale application of the emulator beyond verification tests with the 3D-HST catalogs (Mathews et al. 2023), we test its accuracy compared to full FSPS evaluations in Appendix A. We also supply further diagnostics on the photometric residuals in Appendix B. An example of an SED fit is shown in Figure 2.

### 3.2. EAzY

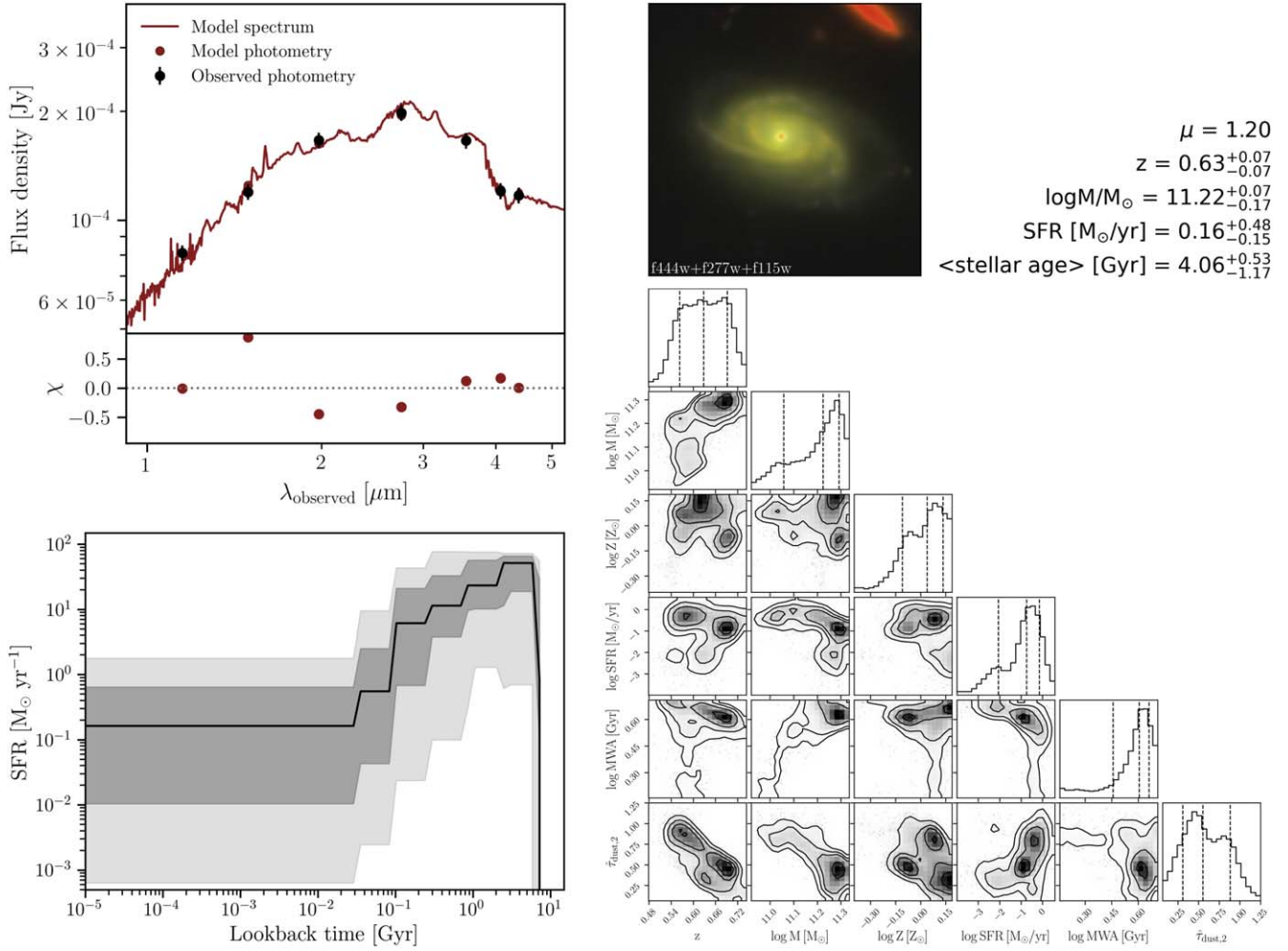
EAzY is a galaxy photometric redshift code that fits the observed SEDs as a nonnegative sum of templates by minimizing the  $\chi^2$  statistics (Brammer et al. 2008). EAzY offers flexibility in fitting different data sets through the modification of templates. We start by the standard publicly available fspss template set, which consists of 12 templates spanning a range of colors. As pointed out by, e.g., Steinhart et al. (2023), the standard method of running EAzY can allow for nonphysical contributions from templates that are older than the age of the Universe at a given redshift, thereby biasing the best fits. The latest sfhz template set is designed to mitigate this problem. Redshift dependence is introduced in the templates so that SFHs starting earlier than the age of the Universe at a given epoch are disallowed. A template from the JWST/NIRSpec observation of a  $z \sim 8$  extreme emission-line galaxy is also added in this set (Carnall et al. 2023), in order to expand the template set to include the more exotic emission-line contributions that have been observed at the highest redshifts.

In consistency with the EAzY settings in Weaver et al. (2024), we turn off the priors on the magnitude and the UV slope. We do not apply the usual methodology of an iterative application of photometric zero-point offsets either. The agreement between the spectroscopic and photometric redshifts marginally worsens after applying the correction, though we caution that the redshifts in this field have a strong selection function due to the foreground cluster and the relatively low number of spectroscopic redshifts. We defer a full exploration of the photo- $z$  accuracy in this field to future works which will exploit forthcoming medium-band and grism redshifts.

## 4. Inferred Stellar Population Parameters

We now present the parameters contained in our stellar population catalogs, an overview of which is shown in Figure 1. Here we also compare the photometric redshifts

<sup>38</sup> The version used in this work is v1.1, which incorporates new observational constraints bringing the lens plane image reproduction rms of the model down to  $\Delta_{\text{RMS}} = 0''.51$ .



**Figure 2.** An example from the UNCOVER field. The upper left shows the SED of a galaxy. The observed photometry is plotted as black dots, while the maximum-likelihood photometry and spectrum are shown in red. The lower left shows the inferred SFH of the galaxy. The  $x$ -axis is the lookback time in gigayears, and the  $y$ -axis is the SFR in units of  $M_{\odot} \text{ yr}^{-1}$ . The RGB color composite is made from the F444W, F277W, and F115W bands. The lower right is a corner plot showing the marginal and joint posterior distributions of redshift, stellar mass, stellar metallicity, SFR, mass-weighted age, and optical depth of the diffuse dust.

inferred using *Prospector- $\beta$* , *EAzY-sfhz*, and *EAzY-fsps* as a quality check.

#### 4.1. Photometric Redshifts

We show a comparison between our recovered photometric redshifts and available spectroscopic redshifts in Figure 3. The scatter in the residuals is quantified using the normalized median absolute deviation (NMAD; Hoaglin et al. 1983) given its advantage of being less sensitive to outliers than standard indicators, e.g., rms. It is defined as

$$\sigma_{\text{NMAD}} = 1.48 \times \text{median}|\Delta z|, \quad (3)$$

where  $\Delta z = (z_{\text{phot}} - z_{\text{spec}})/(1 + z_{\text{spec}})$ . We additionally quantify the outlier fraction,  $f_{\text{out}}$ , in which we define a catastrophic outlier as one with  $|\Delta z| > 0.15$ , and bias calculated using the mean bias error (MBE) as

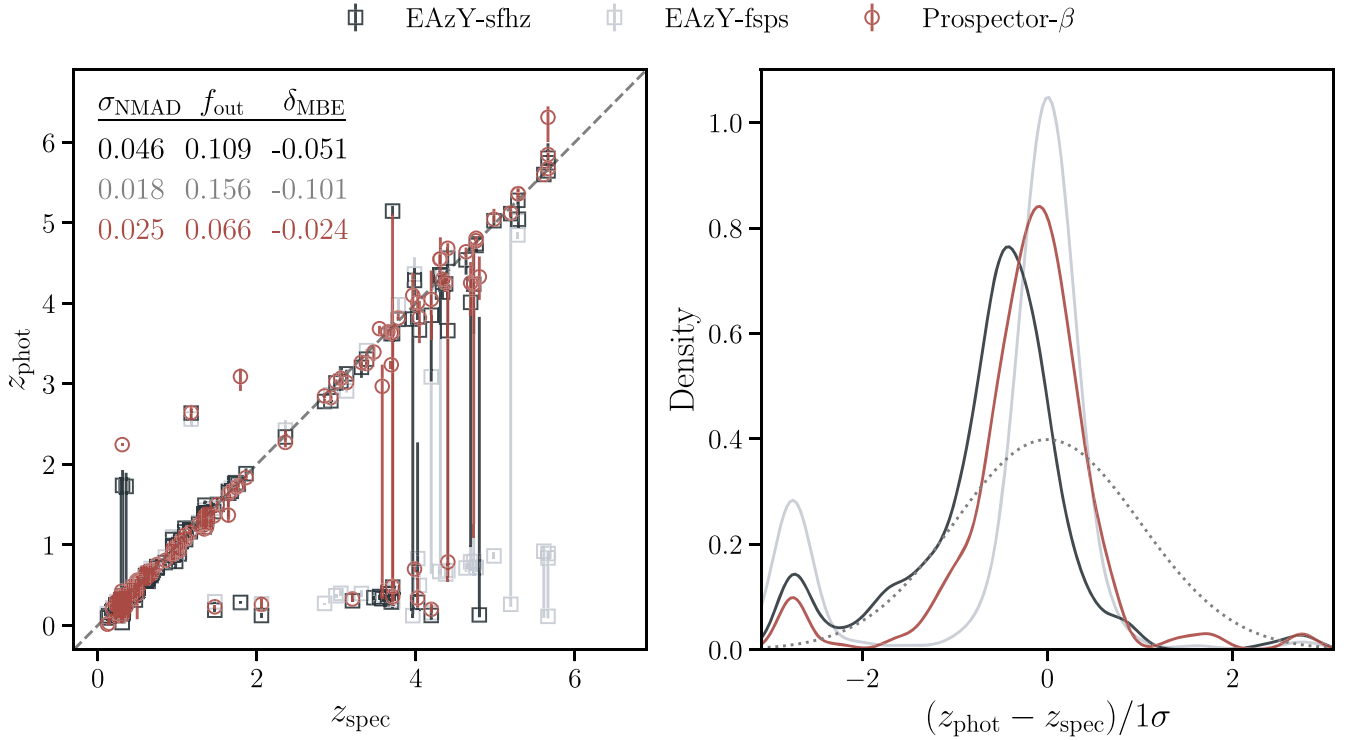
$$\delta_{\text{MBE}} = \frac{1}{n} \sum_{i=1}^n \Delta z. \quad (4)$$

Overall, *Prospector- $\beta$*  performs favorably. *EAzY*'s performance depends on the adopted template set: the *fsps* template set has a low scatter but a high outlier fraction, while

the *sfhz* template has a middle-of-the-road performance in both. This template-dependent performance from *EAzY* is liable to change further as the photometric extraction is improved, and more generally template-based fitting appears to be more sensitive to the choices made during photometric catalog construction. Importantly, as the spectroscopic sample unavoidably has a strong selection bias, we caution not to overinterpolate these results.

We proceed to compare the photometric redshifts from *Prospector- $\beta$* , *EAzY-sfhz*, and *EAzY-fsps* in Figure 4. For the ease of comparing the statistics, we take the results from *Prospector- $\beta$*  as the reference point; that is,  $\Delta z = (z_{\text{EAzY}} - z_{\text{Prospector-}\beta})/(1 + z_{\text{Prospector-}\beta})$ . *EAzY-sfhz* notably produces smaller scatter and bias than *EAzY-fsps* when comparing to the *Prospector- $\beta$*  redshifts, although both agree reasonably well on a high signal-to-noise ratio (S/N) subsample. The agreement deteriorates, however, when all the reliable photometric data are included. As seen in the lower panel of Figure 4, break confusion is not the main cause. Combining with the findings from the spectroscopic sample, model mismatch is a more likely explanation. The scheduled spectroscopic observations of UNCOVER will allow for a more definitive conclusion.





**Figure 3.** Accuracy of the photometric redshifts. Left: the photometric redshifts inferred from the three different settings described in Section 3 are plotted against known spectroscopic redshifts. Also included are the summary statistics quantifying the scatter ( $\sigma_{\text{NMAD}}$ ; Equation (3)), outlier fraction ( $f_{\text{out}}(|\Delta z| > 0.15)$ ), and bias ( $\delta_{\text{MBE}}$ ; Equation (4)). These statistics suggest that we can achieve high-quality redshifts for bright objects. Right: the distributions of photometric redshift residuals normalized by the  $1\sigma$  width of the posteriors are illustrated by kernel density estimations. A unit Gaussian is overplotted as a gray dashed curve to guide the eye. The data are clipped to be within  $3\sigma$  of the unit Gaussian. This calibration plot suggests that all three codes tend to overestimate the uncertainties of typical objects and underestimate the uncertainties of outliers.

The existence of  $z \gtrsim 9$  sources in this catalog is apparent in both Figures 1 and 4. Possible contamination from lower-redshift objects and artifacts is discussed in Section 5.1. An analysis of the modeling uncertainties of a  $z \gtrsim 9$  sample, selected based on redshift posterior distributions contained in the catalog of this paper, is presented in Wang et al. (2023b). This is complementary to the study of a color-selected sample in the UNCOVER field, in which different photometric catalog and SED fitting methods are used (Atek et al. 2023).

#### 4.2. Stellar Masses and Other Ancillary Parameters

In addition to photometric redshifts, we also release stellar masses and other ancillary parameters as listed in Table 2. Stellar mass can often be robustly constrained by photometry; however, extra uncertainties are introduced by varying redshifts and magnifications. Lens models, especially for highly magnified regions, can be uncertain due to systematics (Acebron et al. 2017; Bouwens et al. 2017; Meneghetti et al. 2017; Acebron et al. 2018; Atek et al. 2018; Furtak et al. 2021). Therefore, the uncertainties in magnifications, which are not included in this catalog, can be significant (see Furtak et al. 2023 for the uncertainties in the lens model used in this work). We expect to incorporate fully the lensing uncertainties in the next generations of catalogs.

#### 4.3. Rest-frame Colors

Considering the common practice of using rest-frame colors to categorize star-forming and quiescent galaxies (e.g., Williams et al. 2009; Brammer et al. 2011), we provide rest-

frame fluxes in *UVJ* filters, and also fluxes in the recently proposed synthetic *ugi* filters (Antwi-Danso et al. 2023), both of which are marginalized over the full *Prospector- $\beta$*  posteriors. We show the *UVJ* and *ugi* color-color diagrams in redshift bins where the data have constraining power on the respective colors in Figure 5. Specifically, we only show the *UVJ* colors for galaxies in the following redshift ranges:

1.  $z_{\text{phot}} > 1$ , if optical data (HST F606W/F814W) exist,
2.  $z_{\text{phot}} > 2.3$ , otherwise,
3.  $z_{\text{phot}} < 4$ .

Likewise we only show the *ugi* colors for galaxies in the following redshift ranges:

1.  $z_{\text{phot}} > 1.4$ , if optical data (HST F606W/F814W) exist,
2.  $z_{\text{phot}} > 3.1$ , otherwise,
3.  $z_{\text{phot}} < 6$ .

These colors are, however, provided for all objects in the catalog, including cases where extrapolations are necessary.

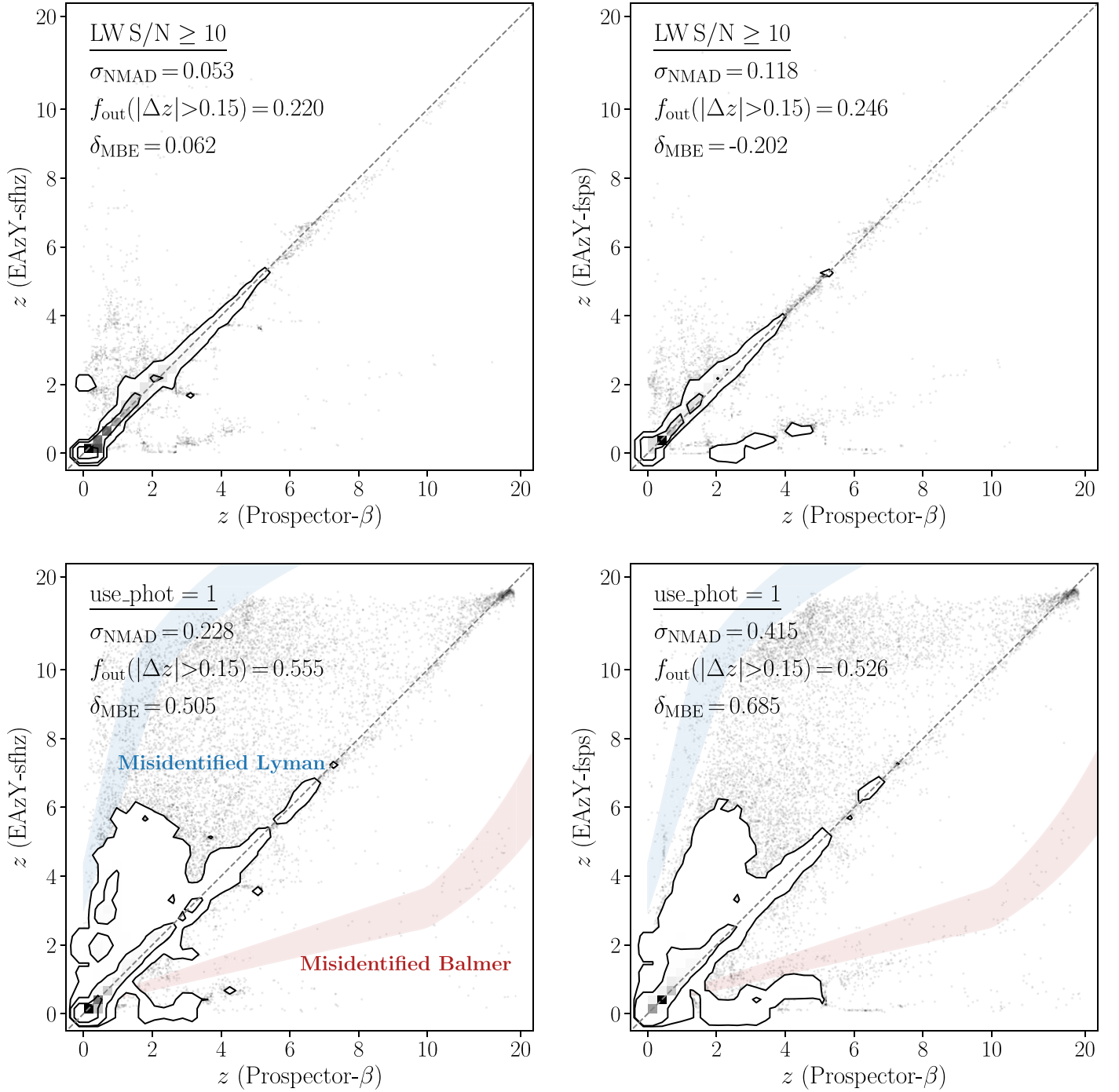
The *UVJ* color-selection criteria for quiescent galaxies are

$$\begin{aligned} (U - V) > 1.23 \wedge (V - J) < 1.67 \wedge \\ (U - V) > (V - J) \times 0.98 + 0.38, \end{aligned} \quad (5)$$

whereas the synthetic *ugi* color-selection criteria are

$$\begin{aligned} (u - g) > 1.5 \wedge (g - i) < 1.8 \wedge \\ (u - g) > (g - i) \times 0.73 + 1.08. \end{aligned} \quad (6)$$

Both equations are taken from Antwi-Danso et al. (2023). The synthetic *ugi* colors are notably better correlated with sSFR at



**Figure 4.** Comparison between EAZY and *Prospector* redshifts. Upper panel: photometric redshifts inferred from *Prospector*- $\beta$  are plotted against those fitted using the latest template set EAZY-sfhz and the standard template set EAZY-fsps, respectively. Here only a subset satisfying  $S/N \geq 10$  in the long-wavelength (LW) detection bands (F277W, F356W, and F444W) is shown. All the statistics are computed by taking the *Prospector*- $\beta$  redshifts as “truth” for the ease of comparison. The scales on both axes are switched from linear to logarithmic at  $z = 10$ . Lower panel: similar to the upper panel, but the photometric redshifts from the full set of sources with reliable photometry are included (i.e.,  $use\_phot = 1$ ). Break confusions (a combination of Balmer, 4000 Å, Ly $\alpha$ , and Lyman continuum) are indicated by the colored shades.

$1.5 \lesssim z \lesssim 3$ , which suggests that they may be a suitably complementary diagnostic for JWST observations. We provide further discussion on the color uncertainties and the utility of rest-frame colors calculated from the best-fit model versus posterior-averaged quantities in Appendix C.

As a validation of the photometric modeling, we select a sample of  $z > 2$  quiescent candidates and cross-match to a sample of spectroscopically confirmed quiescent galaxies

within A2744 (Marchesini et al. 2023). We choose a redshift-dependent definition of quiescence, calculated using a mass doubling number as

$$\mathcal{D}(z) = sSFR_{100}(z) \times t_H(z), \quad (7)$$

which is the number of times the stellar mass doubles within the age of the Universe at redshift  $z$ ,  $t_H(z)$ , at the current sSFR (Tacchella et al. 2022). Focusing on the  $z > 2$  population, we

**Table 2**  
Catalog Columns

Column Name	Description
id	unique identifier; same as in the DR2 photometric catalog (Weaver et al. 2024)
ra	R.A. J2000 [degrees]
dec	decl. J2000 [degrees]
z_spec	spectroscopic redshift, where available; not including any UNCOVER MSA spec-z
z_16/50/84	redshift posterior percentiles, e.g., z16 $\rightarrow$ 16%
mstar_16/50/84	stellar mass [ $\log M_{\odot}$ ]
mwa_16/50/84	mass-weighted age [gigayears]
sfrx_16/50/84	SFR averaged over the most recent $x \sim (x = 10, 30, 100)$ Myr [ $M_{\odot} \text{ yr}^{-1}$ ]
ssfrx_16/50/84	sSFR averaged over the most recent $x \sim (x = 10, 30, 100)$ Myr [ $\text{yr}^{-1}$ ]
met_16/50/84	stellar metallicity [ $\log Z_{\odot}$ ]
dust2_16/50/84	optical depth of diffuse dust
dust1_fraction_16/50/84	ratio between the optical depth of birth cloud dust and diffuse dust
dust_index_16/50/84	power-law index for a Calzetti et al. (2000) attenuation curve
fagn_16/50/84	ratio between the object's AGN luminosity and its bolometric luminosity
rest_U_16/50/84	rest-frame $U$ -band flux [AB mag]
rest_V_16/50/84	rest-frame $V$ -band flux [AB mag]
rest_J_16/50/84	rest-frame $J$ -band flux [AB mag]
rest_u_16/50/84	rest-frame synthetic $u$ -band flux [AB mag]
rest_g_16/50/84	rest-frame synthetic $g$ -band flux [AB mag]
rest_i_16/50/84	rest-frame synthetic $i$ -band flux [AB mag]
UV_16/50/84	rest-frame $U - V$ [AB mag]
VJ_16/50/84	rest-frame $V - J$ [AB mag]
ug_16/50/84	rest-frame synthetic $u - g$ [AB mag]
gi_16/50/84	rest-frame synthetic $g - i$ [AB mag]
chi2	best-fit $\chi^2$ , assuming a minimum error of 5%
nbands	number of bands used in the fit
mu	best-fit magnification based on $z_{50} = 1$ for foreground objects (Furtak et al. 2023)
mu_16/84	magnification uncertainty percentiles; not containing the uncertainty from the $z$ posterior distributions
mu_r	best-fit radial magnification
mu_r_16/84	radial magnification uncertainty percentiles
mu_t	best-fit tangential magnification
mu_t_16/84	tangential magnification uncertainty percentiles
gamma1	best-fit shear_1; total shear $\gamma = \sqrt{\gamma_1^2 + \gamma_2^2}$
gamma1_16/84	uncertainty percentiles
gamma2	best-fit shear_2
gamma2_16/84	uncertainty percentiles
z_eazy	peak of $p(z)$ from EAZY-sfHz
z_eazy_16/50/84	$p(z)$ percentiles
id_DR1	ID of the source corresponding to DR1
id_msa	ID of the source in the MSA catalog (internal release; all within $<0''.24$ radius)
id_alma	ID of ALMA source (Fujimoto et al. 2023a)
flag_kron	1 for systematically underestimated photometry
use_phot	1 if photometry is reliable (F444W S/N $> 3$ , not a star, not likely a bad pixel)
use_aper	arcsecond diameter adopted for color aperture

select our quiescent sample to meet all of the following criteria based on Prospector- $\beta$  outputs:

1. 16th percentile of the redshift posteriors  $>2$  in the Prospector- $\beta$  fits,
2. 50th percentile of the redshift posteriors  $<9$  in the Prospector- $\beta$  fits, and
3.  $\mathcal{D}(z) \leq 1/20$

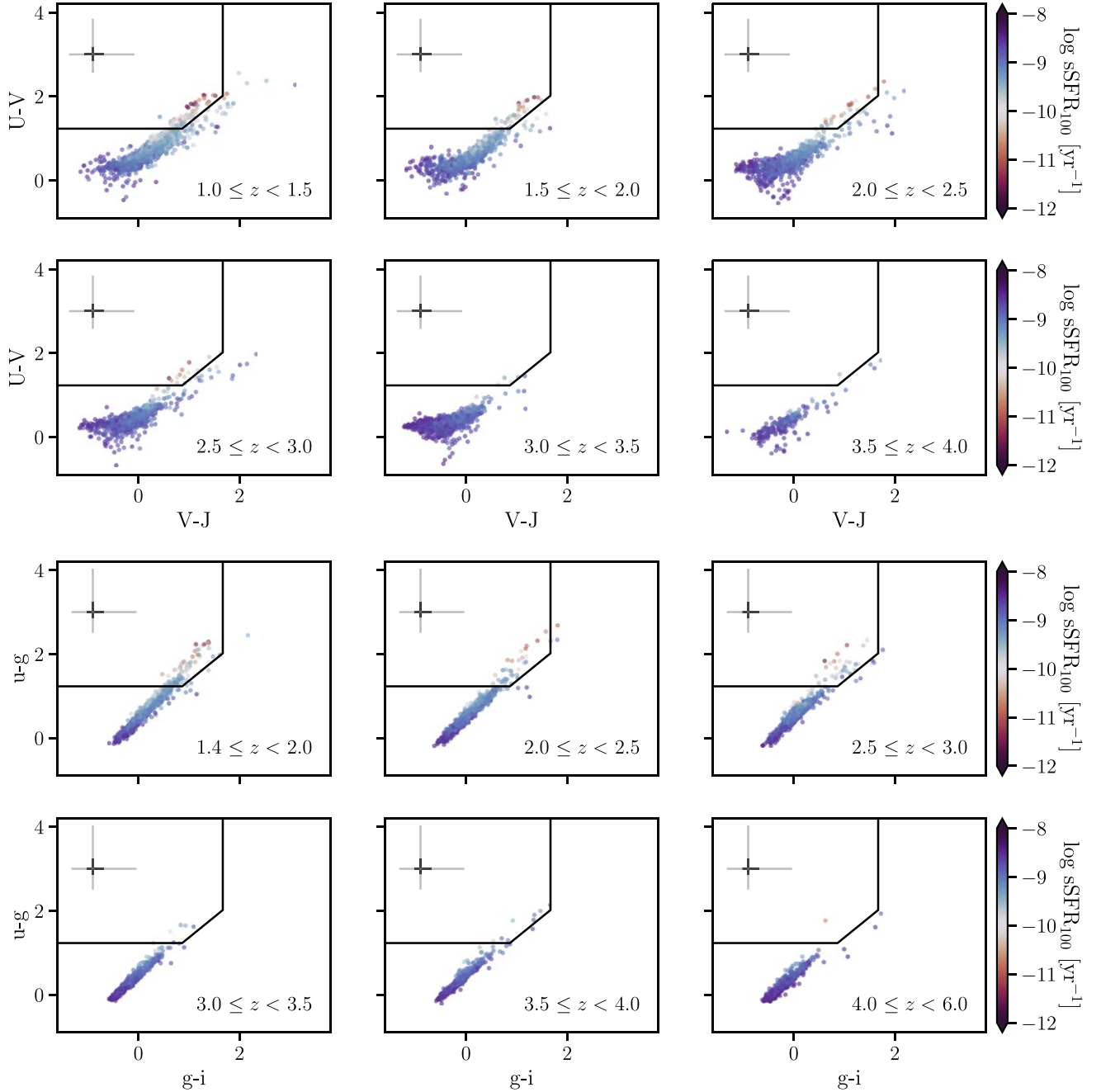
All the candidates passing the above criteria have no data quality issues in the cutouts or SEDs upon visual inspection.

The resulting sample is shown as stars on  $UVJ$  and  $ugi$  color planes in Figure 6. We additionally mark the two spectroscopically confirmed quiescent candidates at  $z > 2$  on the same

figure with squares (Marchesini et al. 2023), both of which are quiescent in our photometric fits.

The implications from Figure 6 are consistent with previous results in the literature: not all quiescent galaxies fall in the rest-frame color-color criteria, and not all galaxies meeting rest-frame color-color criteria are quiescent. This challenge is exacerbated at higher redshifts where all stellar populations are by definition younger and bluer (Leja et al. 2019c; Carnall et al. 2023; Gould et al. 2023). This finding also suggests that full SED fitting can bring additional value for the selection of quiescent galaxies.

A tailored UNCOVER catalog of quiescent candidates based on different selection criteria and model assumptions will be



**Figure 5.** Here we show the rest-frame colors from marginalizing over the *Prospector*- $\beta$  posteriors in redshift bins. The median and the 90% of the uncertainty distributions are shown as black and gray error bars, respectively, in the upper left corner. The asymmetry of the error bars is driven by the non-Gaussianity of the redshift posterior distribution. The galaxies are color coded by sSFR. The synthetic *ugi* colors (lower panel) are notably better correlated with sSFR than the *UVJ* colors (upper panel) at  $1.5 \lesssim z \lesssim 3$ . The best-fit versions of these plots are available in Appendix C.

presented in G. Khullar et al. (2023, in preparation). More dedicated discussions on quiescence can also be found therein.

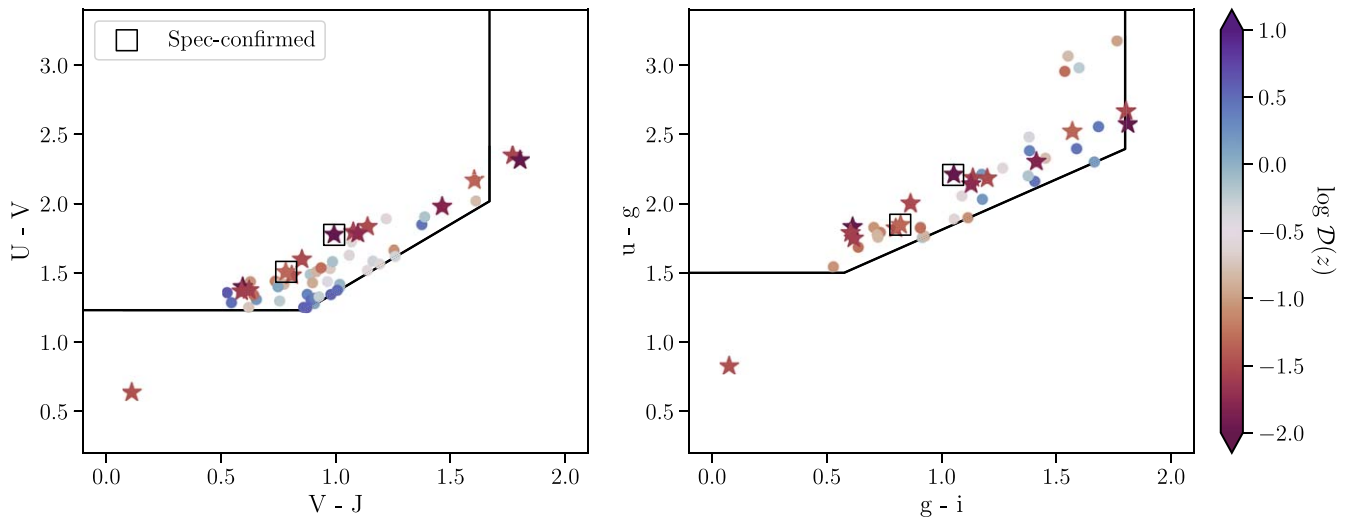
## 5. Known Issues in the Current Data Release and Upcoming Improvements

Thus far, this paper has presented the first-generation galaxy catalog of UNCOVER, derived from photometry that reaches intrinsic depths of  $\gtrsim 31$ – $32$  AB magnitudes after correcting for lensing magnification. We emphasize that the intention of this public release is to make the catalogs available for rapid science and is not intended to be a finalized catalog. Therefore,

the user should be cautioned of the known caveats. In what follows, we discuss the known issues with the photometry and with the SPS models, as well as upcoming improvements.

### 5.1. Known Challenges in the Photometric Catalog

This work is intended to model the photometry as given; that is, it does not attempt to solve possible issues in the first-generation photometric catalogs. Here we discuss the known issues in the context of this work; further details can be found in Weaver et al. (2024).



**Figure 6.** All  $z > 2$  galaxies that satisfy the quiescent criteria of the mass doubling number  $\mathcal{D}(z) \leq 1/20$  are shown as stars on the two color-color planes. Additionally, all  $z > 2$  galaxies that fall into the  $UVJ/ugi$  wedge but have  $\mathcal{D}(z) > 1/20$  are shown as dots. The solid squares indicate the two quiescent galaxies confirmed with NIRISS spectroscopy (Marchesini et al. 2023).

Interpreting early JWST imaging data was made difficult by uncertain photometric calibration. Thanks to efforts across the community, photometric zero-points are now thought to be well understood across the detector to  $<5\%$  (Boyer et al. 2022; see also the photometric calibration presented in the methods section of Labbé et al. 2023).

However, we are still in the early stages of understanding and improving the known artifacts in JWST imaging (Rigby et al. 2023). These include “claws” and “snowballs,” as well as hot pixels that are particularly persistent in LW bands near the detector edges. Unidentified, these artifacts can masquerade as high-redshift galaxies, or cause spurious signals that leads to genuine high-redshift galaxies being misclassified. Such issues are difficult to identify from photometry alone, and so complicate spectral fitting. Significant effort has been expended by our team to remove these features at the reduction level; as such these issues are largely resolved in our most recent image reduction (Bezanson et al. 2022) and photometric catalog (Weaver et al. 2024).

The final known issue worth discussion is that subtracting the brightest cluster galaxies leads to spurious detections of residual features. We conservatively flag objects within  $3''$  of all subtracted cluster galaxy centers. However, there may remain a number of spurious sources at larger radii that are difficult to flag without simultaneously flagging robust sources. While the photometry and spectral fit of such sources may look reasonable, it is obvious when inspecting the image stamps that these sources are artifacts. While it is good practice to inspect the images of any exciting target, we especially encourage this for sources in the immediate vicinity of the three cluster cores.

### 5.2. Known Unknowns in the Modeling

SPS models require many ingredients, including an IMF, isochrones, and stellar spectra for the construction of SSPs; SFHs and stellar metallicity models for the construction of CSPs; a model for dust attenuation and emission, and nebular continuum and line emission (see Walcher et al. 2011; Conroy 2013 for recent reviews). Comprehensive assessments of SED fitting, based on data of exquisite quality and wavelength coverage at  $z \lesssim 3$ , have already highlighted the

dependence of inferred parameters on modeling assumptions (Pacifci et al. 2023). In this work, we infer a panoramic view of the galaxy population out to  $z \sim 15$ , reaching a parameter space where robust theoretical models have yet to undergo robust tests. Accordingly, we discuss a few salient points on the known unknowns in the stellar populations modeling in this section.

The stellar templates are particularly uncertain at high stellar masses and at low metallicities (e.g., Johnson et al. 2021). The evolution of massive stars is strongly affected by the choice of input physics, including the treatment of convection, close binary evolution, rotation effects, and mass loss, each of which has its own uncertainties (Leitherer et al. 1999; Choi et al. 2016; Eldridge et al. 2017; Stanway & Eldridge 2018; Byrne et al. 2022). More importantly, current models assume a solar abundance pattern by necessity, but high-resolution spectra of quiescent galaxies have revealed variations in  $\alpha$ -element abundances (Thomas et al. 2005; Choi et al. 2014; Conroy et al. 2014; Onodera et al. 2015; Kriek et al. 2016). These trends in abundance patterns can change the fluxes by 10–40% (Vazdekis et al. 2015; Choi et al. 2019). As for metallicity histories, we follow the established methodologies in the field that the same metallicity is assumed across different bins in the SFH (Mitchell et al. 2013; Webb et al. 2020; Tacchella et al. 2022). Although a possible time dependence has been claimed (Bellstedt et al. 2021; Thorne et al. 2022), we think that our approach is adequate for this work because the catalog is dominated by high-redshift, low-mass objects. These objects tends to have rising SFHs, whereas the metallicity histories are most impactful for star-forming objects with falling SFHs. While the exact effects of the aforementioned uncertainties on SED modeling remain unclear, they can be partly illustrated by the disparate solutions found when using different stellar templates, a variety of which exist in the literature. Those templates cover different ranges of stellar evolutionary tracks and isochrones. In some cases, it has been shown that the different choices (e.g., MIST versus PARSEC in Whittler et al. 2023) can lead to the inferred stellar ages differing by up to an order of magnitude.

Nebular emission can make up a significant fraction of the total flux for stars at low metallicity and at young ages (Anders

& Fritze-v. Alvensleben 2003). This alone means that it plays an outsize importance at high redshifts (e.g., Smit et al. 2014). Nebular emission also becomes increasingly important at high redshifts for a more technical reason: the redshifting of the spectrum causes a feature with a fixed rest-frame equivalent width to occupy a larger fraction of the filter bandpass. It is a known challenge to model nebular emission in the early Universe, due to a complex combination of nonsolar abundance patterns, large uncertainties in the incident ionizing radiation, and high densities of both gas and ionizing photons (Schaerer & de Barros 2009; Stark et al. 2013; de Barros et al. 2014; Gutkin et al. 2016; Steidel et al. 2016; Byler et al. 2017; Strom et al. 2018; Freeman et al. 2019). Wang et al. (2023b) estimate the systematic uncertainty driven by nebular physics in the inferred galaxy properties by employing a flexible nebular emission model, and find a  $\sim 0.2$  dex systematic increase in stellar mass.

The initial distribution of masses for a population of stars (i.e., IMF), influences almost all the inferred properties of the stellar population—mostly notably, the total luminosity and total stellar mass. Various theories predict different shapes of the IMF (e.g., Salpeter 1955; Kroupa 2001; Chabrier 2003). While it is typically assumed to be constant, there is emerging evidence that it varies across time and environment (Conroy & van Dokkum 2012; La Barbera et al. 2013; Spiniello et al. 2014; Lyubenova et al. 2016; Lagattuta et al. 2017; van Dokkum et al. 2017). The recently proposed temperature dependence in the IMF (Steinhardt et al. 2023) and variations in low-metallicity environments (Chon et al. 2021, 2022) may lead to a systematic departure from this universality, particularly at high redshifts. Here we assume a fixed Chabrier (2003) IMF, and caution that the inferred SFRs and stellar masses can vary by up to a factor of 10 based on this assumption (Wang et al. 2023b).

It is worth noting that the aforementioned systematic issues apply to all SED fitting. The inflow of JWST data breathes new life into model fitting and interpretation, as is evident from the active discussion in the literature (Topping et al. 2022; Adams et al. 2023; Ferrara et al. 2023; Kannan et al. 2023; Mauerhofer & Dayal 2023; Mirocha & Furlanetto 2023; Reddy et al. 2023; Yung et al. 2024). The effects of varying SPS model assumptions including burstiness in SFH, non-Universal IMF, and nebular physics, using data from this catalog, are examined in detail in Wang et al. (2023b).

### 5.3. Reliability of the Photometric Redshifts and Future Improvements

Given the extensive discussion on inferring photometric redshifts in the literature (see Newman & Gruen 2022 for a recent review; and Alsing et al. 2023 and Leistedt et al. 2023 for general discussions on photometric redshift inference), we focus only on the unique issues faced in this work below.

Considerable uncertainties exist in the lens models, including systematic uncertainties between different models and in the highly magnified regions within a model (e.g., Zitrin et al. 2015). Additionally, we note that the lensing maps do not cover our entire field of view, and thus all sources that fall outside of the lensing maps are assigned  $\mu = 1$ . In reality the peripheral areas can be magnified by  $\mu \lesssim 1.3$ . A complete set of lensing maps will be released in the future. The full effect of magnification uncertainties on the redshifts and other parameters will also be studied, where we add  $\mu$  as a free parameter

with an informative prior from the lensing maps in the SED fitting.

Most photometric redshift information comes from the positions of spectral breaks, e.g., the dropout technique (Steidel et al. 1996). In principle, all high-redshift objects, with a specific wavelength coverage and high-S/N images taken across multiple bands, are detectable via this technique. An obvious concern is the possible contamination from low- $z$  objects exhibiting breaks in similar locations. In particular, it can be challenging to distinguish between a Balmer break and strong emission lines (Dunlop et al. 2007; Naidu et al. 2022; Arrabal Haro et al. 2023; McKinney et al. 2023; Zavala et al. 2023). This degeneracy is mitigated, but not removed, by the adoption of the mass function prior in `Prospector- $\beta$` .

Further uncertainties in the inferred photometric redshifts come from modeling  $\text{Ly}\alpha$  and its interaction with the IGM. The emulator used in this work (Mathews et al. 2023) is trained on a `Cloudy` grid (Byler et al. 2017), and hence does not accurately account for the radiative transfer process (e.g., damping wings). We defer a careful modeling of  $\text{Ly}\alpha$  to future works.

Observationally, increasing the wavelength coverage or resolution will improve the accuracy as well as the precision of the inferred redshifts. The A2744 field will be observed with all the JWST medium bands during Cycle 2 (PI: Suess, JWST-GO-4111). These observations are expected to be especially helpful in determining the uncertain emission-line contribution. On the modeling side, further improvements will come from an accurate estimation of the detection efficiency as a function of mass based on the flux limits in the photometry. This will inform our model about the survey volume and downweigh spurious high-redshift solutions.

Taken together, we have put our best effort forward to create the first-look catalogs. For the photometric catalogs, Weaver et al. (2024) calibrate the photometry and remove known spurious sources as cleanly as possible; for the stellar population catalogs of this paper, we adopt a full Bayesian approach, incorporating empirical priors and correcting for magnification during model fitting, to ensure the maximum science return from the early observations. However, we again caution the reader to have a healthy level of skepticism in working with first-generation JWST data, especially when using sources in more exotic parameter spaces.

## 6. Summary

In this paper, we present a first-generation galaxy catalog spanning  $0.2 \lesssim z \lesssim 15$ , as part of the public release from the JWST extragalactic Treasury survey, UNCOVER. We adopt the `Prospector` Bayesian inference framework (Johnson et al. 2021), within which we use the nonparametric SFH model in `Prospector- $\alpha$`  (Leja et al. 2019a), and three observationally motivated priors on the stellar mass functions, stellar metallicities, and SFHs in `Prospector- $\beta$`  (Wang et al. 2023c). We constrain redshifts and galaxy properties simultaneously, meaning that the commonly non-Gaussian redshift uncertainties are propagated into the inferred properties of the galaxy population. We treat lensing magnification consistently within `Prospector`, in contrast to the conventional approach where models are corrected for magnification postfit.

This paper is accompanied by a catalog which is derived from the photometric supercatalog assembled using adaptive aperture sizes (Weaver et al. 2024). The UNCOVER SPS catalog contains the 16th, 50th, and 84th quantiles of the

posterior distributions modeled with `Prospector- $\beta$`  for redshift, stellar mass, mass-weighted age, SFR, sSFR, stellar metallicity, optical depth of diffuse dust, ratio between the optical depth of birth cloud dust and diffuse dust, power-law index for a Calzetti et al. (2000) attenuation curve, and the ratio between the object’s AGN luminosity and its bolometric luminosity. Analytic estimates of magnifications, based on the redshift posterior medians, along with radial and tangential magnifications and shears are supplied for detailed lensing analyses (Furtak et al. 2023). Complementary redshifts from `EAZy` are included as well. An explanation of the catalog columns can be found in Table 2. We additionally provide the maximum-likelihood spectra, SFHs, and full posterior distributions. The catalog and all related documentation are accessible via the UNCOVER survey webpage<sup>39</sup> with a copy deposited on Zenodo at doi:10.5281/zenodo.8401181.

Future updates to the stellar population catalog are expected in accordance with releases of extended photometric and/or spectroscopic data. The main planned enhancements in parameter inference are the incorporation of a number density prior, and lensing magnification as a free parameter with informative priors from the lens model.

We conclude by reiterating that the UNCOVER survey provides the deepest view into our Universe to date by targeting the strong lens cluster A2744. The stellar population catalog presented in this paper offers a rich data set to explore the processes governing galaxy formation and evolution over a redshift range now accessible by JWST.

### Acknowledgments

This work is based in part on observations made with the NASA/ESA/CSA James Webb Space Telescope. The data were obtained from the Mikulski Archive for Space Telescopes at the Space Telescope Science Institute, which is operated by the Association of Universities for Research in Astronomy, Inc. (AURA), under NASA contract NAS 5-03127 for JWST. These observations are associated with JWST-GO-2561, JWST-ERS-1324, and JWST-DD-2756. Support for program JWST-GO-2561 was provided by NASA through a grant from the Space Telescope Science Institute under NASA contract NAS 526555. This research is also based on observations made with the NASA/ESA Hubble Space Telescope obtained from the Space Telescope Science Institute under NASA contract NAS 526555. These observations are associated with programs HST-GO-11689, HST-GO-13386, HST-GO/DD-13495, HST-GO-13389, HST-GO-15117, and HST-GO/DD-17231. The specific observations included in the JWST/UNCOVER first epoch survey data can be accessed via 10.17909/zn4s-0243, whereas the full list of HST/JWST observations used to produce our UNCOVER catalogs is available via 10.17909/nftp-e621.

B.W. thanks the Penn State Institute for Gravitation and the Cosmos for financial support during the course of this work. R. B. acknowledges support from the Research Corporation for Scientific Advancement (RCSA) Cottrell Scholar Award ID No. 27587. L.F. and A.Z. acknowledge support by grant No. 2020750 from the United States–Israel Binational Science Foundation (BSF) and grant No. 2109066 from the United States National Science Foundation (NSF), and by the Ministry of Science & Technology, Israel. P.D. acknowledges support

from NWO grant 016.VIDI.189.162 (“ODIN”) and from the European Commission’s and University of Groningen’s CO-FUND Rosalind Franklin program. H.A. acknowledges support from CNES (Centre National d’Etudes Spatiales). R.S. acknowledges an STFC Ernest Rutherford Fellowship (ST/S004831/1). M.S. acknowledges support from the CIDE-GENT/2021/059 grant, from project PID2019-109592GB-I00/AEI/10.13039/501100011033 from the Spanish Ministerio de Ciencia e Innovación—Agencia Estatal de Investigación, and from Proyecto ASFAE/2022/025 del Ministerio de Ciencia y Innovación en el marco del Plan de Recuperación, Transformación y Resiliencia del Gobierno de España. The work of C.C.W. is supported by NOIRLab, which is managed by the AURA under a cooperative agreement with the NSF.

Computations for this research were performed on the Pennsylvania State University’s Institute for Computational and Data Sciences’ Roar supercomputer. This publication made use of the NASA Astrophysical Data System for bibliographic information.

*Facilities:* HST (ACS, WFC3), and JWST (NIRCam, NIRSpec).

*Software:* Astropy (Astropy Collaboration et al. 2013, 2018, 2022), Corner (Foreman-Mackey 2016), EAZy (Brammer et al. 2008), Dynesty (Speagle 2020), Matplotlib (Hunter 2007), NumPy (Harris et al. 2020), Prospector (Johnson et al. 2021), and SciPy (Virtanen et al. 2020).

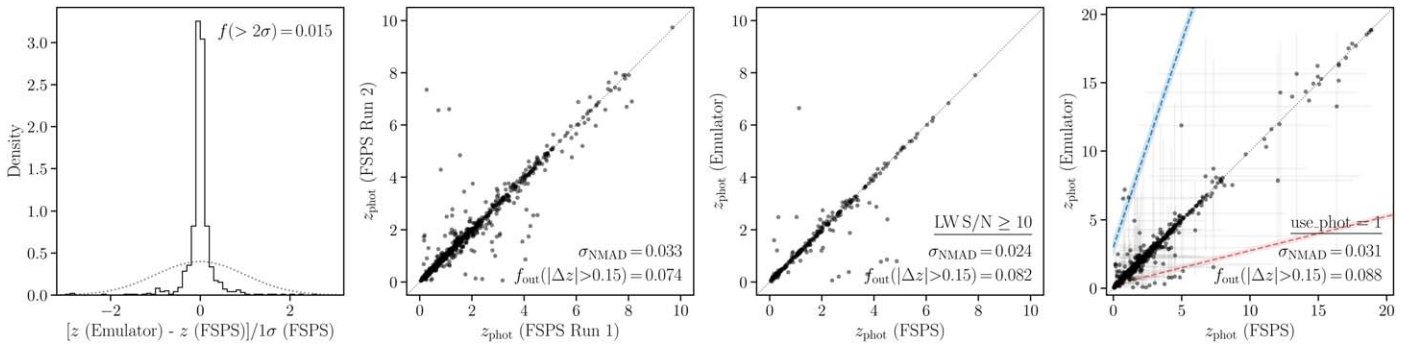
## Appendix A

### Accuracy of Parameters Inferred with the Neural Net Emulator

This work is the first large-scale application of the neural net emulator for SPS, dubbed `parrot` (Mathews et al. 2023), which necessitates an assessment of its accuracy in inferring parameters. Mathews et al. (2023) discusses this accuracy in both flux space and in inferred parameter space but only with fixed redshifts; a free redshift significantly complexifies the parameter space by adding multiple new posterior modes, and so in this appendix we examine the accuracy of the emulator in this new mode. We emphasize that at peak performance, the neural net emulator will exactly replicate the FSPS results, modulo any uncertainty introduced during the sampling process by the probabilistic nature of sampling.

We randomly draw 1000 objects from the full UNCOVER sample and refit them with FSPS (Conroy & Gunn 2010). The accuracy of the most important and challenging parameter, redshift, is assessed in four aspects summarized in Figure A1. First, we calculate the difference between the emulator and FSPS redshifts normalized by the  $1\sigma$  width in the FSPS posterior distribution. In general, we find the emulator performs well in this test. The great majority of the inferred photometric redshifts is within  $1\sigma$  of the full fits, with the fraction of  $>2\sigma$  outliers being 0.015. Although the ideal performance is a  $\delta$  function, the actual distribution of normalized residuals suggests that the emulator is well calibrated. Second, we run FSPS twice with identical settings to estimate the sampling uncertainty. The sampling method used is nested sampling (Skilling 2004), which is better suited to sample multimodal posteriors than other traditional techniques such as Markov Chain Monte Carlo (Goodman & Weare 2010). However, it has also been shown that nested sampling does not always accurately sample the global minimum when fitting for galaxy redshifts (Wang et al. 2023d). Our finding is consistent with

<sup>39</sup> <https://jwst-uncover.github.io/DR2.html#SPSCatalogs>



**Figure A1.** Comparison between the emulator and the FSPS redshifts on a sample of 1000 randomly drawn objects from the full UNCOVER catalog. These plots suggest that the emulator is well calibrated, and the difference is captured in the uncertainties reported in the catalog. (a) Shown here is the distribution of the difference between the emulator and FSPS redshifts normalized by the  $1\sigma$  width of the FSPS posterior distribution. A unit Gaussian is overplotted as a dotted line. The fraction of  $>2\sigma$  outliers is 0.015. (b) Medians of the redshift posteriors from one run using FSPS are plotted against these from a second run under identical settings. Deviation from the diagonal reflects the sampling uncertainty arising from its probabilistic nature. (c) Medians of the redshift posteriors inferred using the emulator are plotted against the medians inferred using FSPS. Only results from a subset where  $S/N \geq 10$  in the LW detection bands are shown. (d) Same as the third panel, but the full validation set is included. Error bars are the 16th–84th quantiles. The Lyman break confusion is indicated in blue, and the shading shows  $\pm 0.2$  in redshift.

this earlier study. In principle, the mode-finding problem in nested sampling can be avoided by substantial increases in the accuracy settings and thus the number of models called. This comes at a cost of increased CPU hours, which quickly becomes prohibitively expensive for large-scale applications. Here we do not attempt to remove the sampling error completely, but instead adopt realistic *dynesty* (Speagle 2020) settings already more strict than those typically used in the literature, which keeps the time per fit roughly under an hour. Third, we compare the emulator and FSPS redshifts on a subsample in which the LW detection bands have  $S/N \geq 10$ . This allows for an examination of the emulator’s performance without the additional complication from data quality issues. The scatter and outlier fraction are comparable to the expectations from the sampling uncertainty, indicating that the emulator agrees well with FSPS on highly confident photometric data. Fourth, we compare the performance on the full validation set. The outlier fraction increases marginally, where the catastrophic outliers roughly follow the lines indicating confusion between a Lyman and a Balmer break.

Given the finding above, we infer that the difference in the redshift posterior distributions found by the emulator and FSPS is mainly caused by a combination of two systematics. First, the emulated fluxes on average have 1%–4% errors compared to the exact FSPS fluxes (Mathews et al. 2023). Second, the sampler struggles to assign a correct posterior mass due to the complex likelihood surface. Fitting early JWST data exacerbates this challenge; in particular in light of the newly emerged model mismatch problem, suggesting photometric calibrations are yet to be complete.

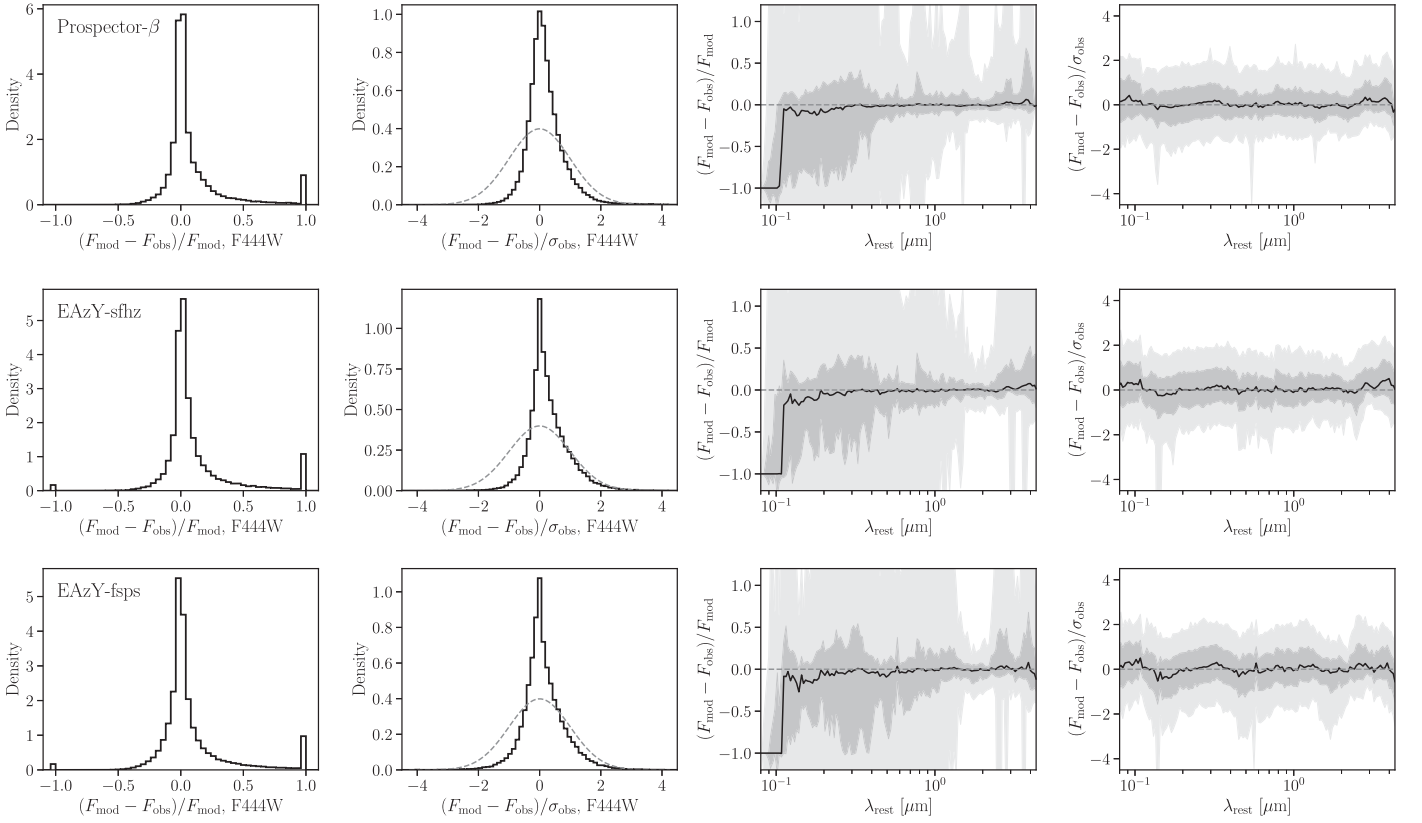
With that being said, the uncertainties on the redshifts in Figure A1 accurately capture the true residuals even in the

presence of emulation errors. Thus, the difference between the emulator and FSPS results are in general well described by the reported uncertainties in the catalog. An additional valuable, independent check on the fidelity of the inferred parameters can likely be obtained via an alternative inference technique, since the latter is affected by different systematics (Wang et al. 2023d), or by comparing to additional spectra. This approach will be examined in the next generations of stellar populations catalogs.

## Appendix B Photometric Residuals

An examination of the residuals between the observed photometry and its maximum-likelihood model offers important insights into the agreement between the data and the model. Figure B1 shows fractional and uncertainty-normalized residuals in the observer and the rest frames. We find general agreement between the *Prospector- $\beta$*  and *EaZY* fits in the observer frame. Deviations from the unit Gaussian in the uncertainty-normalized residuals suggest that the photometry and the associated uncertainty require further refinement. The rest-frame residuals from the *Prospector- $\beta$*  fits fluctuate around 0, which suggests that there is no significant bias in our model templates. The large spikes are likely due to redshift traps, since the model spectra have to be shifted by the inferred redshifts. In contrast, systematic offsets in rest-frame residuals at short wavelengths are observed in the *EaZY-sfhz* and *EaZY-fsps* fits, which may indicate template mismatches. However, given the ongoing efforts in the photometric calibration, we caution against an overinterpretation of the *EaZY* performance at the current stage.



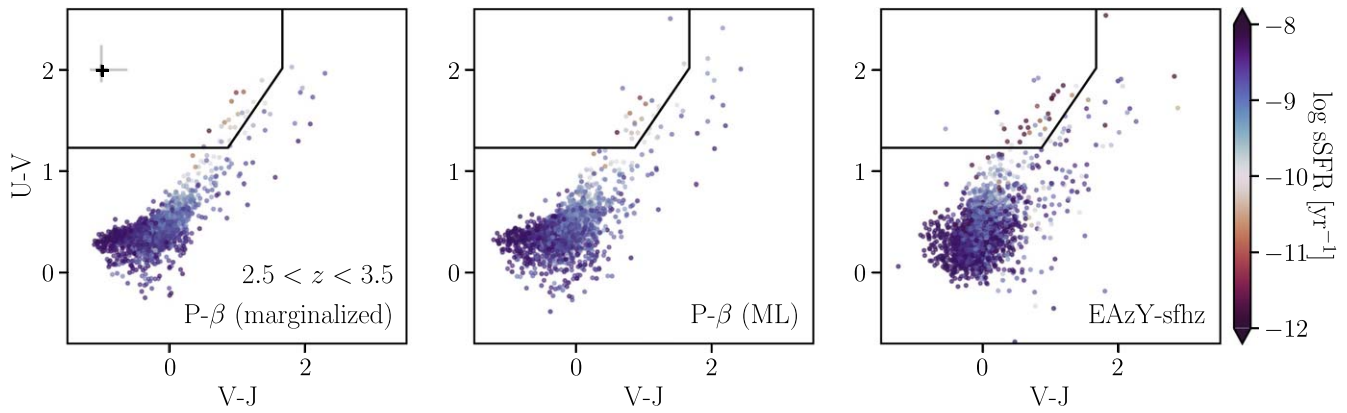


**Figure B1.** The distribution of photometric residuals resulting from *Prospector- $\beta$*  and EAZY fits. We impose a minimum 5% error floor on the photometry. The upper panel shows the following from left to right: (a) fractional residuals in the observer frame, calculated as (modeled flux – observed flux)/(modeled flux) in the F444W band; the data are clipped to  $\pm 1$ ; (b) uncertainty-normalized residuals in the observer frame, calculated as (modeled flux – observed flux)/(uncertainty in observed flux) in the F444W band; the data are clipped to  $\pm 3\sigma$ . The gray dashed line indicates a unit Gaussian for reference; (c) fractional residuals in the rest frame, binned logarithmically in wavelengths; and (d) error-normalized residuals in the rest frame, also binned logarithmically in wavelength. Shaded regions indicate the 16th–84th and the 2.5th–97.5th percentiles. The middle and lower panels respectively show the EAZY-sfhz and EAZY-fsps residuals in the same manner. The *Prospector- $\beta$*  and EAZY fits generally agree. However, with JWST photometric calibrations still ongoing, we caution against an overinterpretation of the performance at the current stage.

### Appendix C Rest-frame Colors

The rest-frame colors released in the catalogs are marginalized over the full *Prospector- $\beta$*  posteriors. Here we additionally show the colors estimated from maximum-likelihood spectra in Figure C1, which have larger scatter as

expected. We also include the colors from EAZY-sfhz. EAZY measures the colors directly from the best-fit template, which is simply a linear combination of templates that minimizes the  $\chi^2$  statistics. Less information is encoded in the process determining the colors this way; it is thus understandable that the EAZY colors exhibit a larger scatter.



**Figure C1.** Here we compare the rest-frame colors of galaxies at  $2.5 < z < 3.5$  inferred by three different methods: marginalizing over the full *Prospector- $\beta$*  posteriors, colors inferred from the maximum-likelihood (ML) spectra from *Prospector- $\beta$* , and from the best-fit templates of *EAZY-sfhz*. The medians of the uncertainty distributions are indicated by black error bars, while the 90% quantiles of the uncertainty distributions are indicated by gray error bars. The asymmetry of the error bars is driven by the non-Gaussianity of the redshift posterior distribution. Only objects which have  $S/N \geq 10$  in the LW detection bands are included for the ease of interpreting the difference. The marginalized colors have a smaller scatter because marginalization tamps down the photometric uncertainties, but their uncertainties are reflective of the larger scatter found by the other two methods.

### ORCID iDs

Bingjie Wang (王冰洁) <https://orcid.org/0000-0001-9269-5046>  
 Joel Leja <https://orcid.org/0000-0001-6755-1315>  
 Ivo Labbé <https://orcid.org/0000-0002-2057-5376>  
 Rachel Bezanson <https://orcid.org/0000-0001-5063-8254>  
 Katherine E. Whitaker <https://orcid.org/0000-0001-7160-3632>  
 Gabriel Brammer <https://orcid.org/0000-0003-2680-005X>  
 Lukas J. Furtak <https://orcid.org/0000-0001-6278-032X>  
 John R. Weaver <https://orcid.org/0000-0003-1614-196X>  
 Sedona H. Price <https://orcid.org/0000-0002-0108-4176>  
 Adi Zitrin <https://orcid.org/0000-0002-0350-4488>  
 Hakim Atek <https://orcid.org/0000-0002-7570-0824>  
 Dan Coe <https://orcid.org/0000-0001-7410-7669>  
 Sam E. Cutler <https://orcid.org/0000-0002-7031-2865>  
 Pratika Dayal <https://orcid.org/0000-0001-8460-1564>  
 Pieter van Dokkum <https://orcid.org/0000-0002-8282-9888>  
 Robert Feldmann <https://orcid.org/0000-0002-1109-1919>  
 Danilo Marchesini <https://orcid.org/0000-0001-9002-3502>  
 Marijn Franx <https://orcid.org/0000-0002-8871-3026>  
 Natascha Förster Schreiber <https://orcid.org/0000-0003-4264-3381>  
 Seiji Fujimoto <https://orcid.org/0000-0001-7201-5066>  
 Marla Geha <https://orcid.org/0000-0002-7007-9725>  
 Karl Glazebrook <https://orcid.org/0000-0002-3254-9044>  
 Anna de Graaff <https://orcid.org/0000-0002-2380-9801>  
 Jenny E. Greene <https://orcid.org/0000-0002-5612-3427>  
 Stéphanie Juneau <https://orcid.org/0000-0002-0000-2394>  
 Susan Kassin <https://orcid.org/0000-0002-3838-8093>  
 Mariska Kriek <https://orcid.org/0000-0002-7613-9872>  
 Gourav Khullar <https://orcid.org/0000-0002-3475-7648>  
 Michael Maseda <https://orcid.org/0000-0003-0695-4414>  
 Lamiya A. Mowla <https://orcid.org/0000-0002-8530-9765>  
 Adam Muzzin <https://orcid.org/0000-0002-9330-9108>  
 Themiya Nanayakkara <https://orcid.org/0000-0003-2804-0648>  
 Erica J. Nelson <https://orcid.org/0000-0002-7524-374X>  
 Pascal A. Oesch <https://orcid.org/0000-0001-5851-6649>  
 Camilla Pacifici <https://orcid.org/0000-0003-4196-0617>  
 Richard Pan <https://orcid.org/0000-0002-9651-5716>

Casey Papovich <https://orcid.org/0000-0001-7503-8482>  
 David J. Setton <https://orcid.org/0000-0003-4075-7393>  
 Alice E. Shapley <https://orcid.org/0000-0003-3509-4855>  
 Renske Smit <https://orcid.org/0000-0001-8034-7802>  
 Mauro Stefanon <https://orcid.org/0000-0001-7768-5309>  
 Katherine A. Suess <https://orcid.org/0000-0002-1714-1905>  
 Edward N. Taylor <https://orcid.org/0000-0002-5522-9107>  
 Christina C. Williams <https://orcid.org/0000-0003-2919-7495>

### References

- Acebron, A., Jullo, E., Limousin, M., et al. 2017, *MNRAS*, 470, 1809  
 Acebron, A., Cibirka, N., Zitrin, A., et al. 2018, *ApJ*, 858, 42  
 Adams, N. J., Conselice, C. J., Ferreira, L., et al. 2023, *MNRAS*, 518, 4755  
 Alsing, J., Peiris, H., Leja, J., et al. 2020, *ApJS*, 249, 5  
 Alsing, J., Peiris, H., Mortlock, D., Leja, J., & Leistedt, B. 2023, *ApJS*, 264, 29  
 Anders, P., & Fritze-v. Alvensleben, U. 2003, *A&A*, 401, 1063  
 AntwiDanso, J., Papovich, C., Leja, J., et al. 2023, *ApJ*, 943, 166  
 Arrabal Haro, P., Dickinson, M., Finkelstein, S. L., et al. 2023, *ApJL*, 951, L22  
 Astropy Collaboration, Price-Whelan, A. M., Lim, P. L., et al. 2022, *ApJ*, 935, 167  
 Astropy Collaboration, Price-Whelan, A. M., Sipőcz, B. M., et al. 2018, *AJ*, 156, 123  
 Astropy Collaboration, Robitaille, T. P., Tollerud, E. J., et al. 2013, *A&A*, 558, A33  
 Atek, H., Chemerynska, I., Wang, B., et al. 2023, *MNRAS*, 524, 5486  
 Atek, H., Richard, J., Kneib, J.-P., & Schaerer, D. 2018, *MNRAS*, 479, 5184  
 Behroozi, P., Wechsler, R. H., Hearin, A. P., & Conroy, C. 2019, *MNRAS*, 488, 3143  
 Bellstedt, S., Robotham, A. S. G., Driver, S. P., et al. 2021, *MNRAS*, 503, 3309  
 Bezanson, R., Labbé, I., Whitaker, K. E., et al. 2022, arXiv:2212.04026  
 Böker, T., Beck, T. L., Birkmann, S. M., et al. 2023, *PASP*, 135, 038001  
 Bouwens, R. J., Oesch, P. A., Illingworth, G. D., Ellis, R. S., & Stefanon, M. 2017, *ApJ*, 843, 129  
 Boyer, M. L., Anderson, J., Gennaro, M., et al. 2022, *RNAAS*, 6, 191  
 Brammer, G. B., Sánchez-Janssen, R., Labbé, I., et al. 2012, *ApJL*, 758, L17  
 Brammer, G. B., van Dokkum, P. G., & Coppi, P. 2008, *ApJ*, 686, 1503  
 Brammer, G. B., Whitaker, K. E., van Dokkum, P. G., et al. 2011, *ApJ*, 739, 24  
 Byler, N., Dalcanton, J. J., Conroy, C., & Johnson, B. D. 2017, *ApJ*, 840, 44  
 Byrne, C. M., Stanway, E. R., Eldridge, J. J., McSwiney, L., & Townsend, O. T. 2022, *MNRAS*, 512, 5329  
 Calzetti, D., Armus, L., Bohlin, R. C., et al. 2000, *ApJ*, 533, 682  
 Carnall, A. C., Begley, R., McLeod, D. J., et al. 2023, *MNRAS*, 518, L45  
 Chabrier, G. 2003, *PASP*, 115, 763  
 Charlot, S., & Fall, S. M. 2000, *ApJ*, 539, 718  
 Choi, J., Conroy, C., & Johnson, B. D. 2019, *ApJ*, 872, 136

- Choi, J., Conroy, C., Moustakas, J., et al. 2014, *ApJ*, 792, 95
- Choi, J., Dotter, A., Conroy, C., et al. 2016, *ApJ*, 823, 102
- Chon, S., Omukai, K., & Schneider, R. 2021, *MNRAS*, 508, 4175
- Chon, S., Ono, H., Omukai, K., & Schneider, R. 2022, *MNRAS*, 514, 4639
- Conroy, C. 2013, *ARA&A*, 51, 393
- Conroy, C., Graves, G. J., & van Dokkum, P. G. 2014, *ApJ*, 780, 33
- Conroy, C., & Gunn, J. E. 2010, *ApJ*, 712, 833
- Conroy, C., & van Dokkum, P. G. 2012, *ApJ*, 760, 71
- Cowie, L. L., Songaila, A., Hu, E. M., & Cohen, J. G. 1996, *AJ*, 112, 839
- de Barros, S., Schaerer, D., & Stark, D. P. 2014, *A&A*, 563, A81
- Dotter, A. 2016, *ApJS*, 222, 8
- Draine, B. T., & Li, A. 2007, *ApJ*, 657, 810
- Dunlop, J. S., Cirasuolo, M., & McLure, R. J. 2007, *MNRAS*, 376, 1054
- Eldridge, J. J., Stanway, E. R., Xiao, L., et al. 2017, *PASA*, 34, e058
- Feldmann, R., Quataert, E., Faucher-Giguère, C.-A., et al. 2023, *MNRAS*, 522, 3831
- Ferrara, A., Pallottini, A., & Dayal, P. 2023, *MNRAS*, 522, 3986
- Finkelstein, S. L., Bagley, M. B., Ferguson, H. C., et al. 2023, *ApJL*, 946, L13
- Foreman-Mackey, D. 2016, *JOSS*, 1, 24
- Freeman, W. R., Siana, B., Kriek, M., et al. 2019, *ApJ*, 873, 102
- Fujimoto, S., Bezanson, R., Labbé, I., et al. 2023a, arXiv:2309.07834
- Fujimoto, S., Wang, B., Weaver, J., et al. 2023b, arXiv:2308.11609
- Furtak, L. J., Atek, H., Lehnert, M. D., Chevillard, J., & Charlot, S. 2021, *MNRAS*, 501, 1568
- Furtak, L. J., Zitrin, A., Weaver, J. R., et al. 2023, *MNRAS*, 523, 4568
- Gallazzi, A., Charlot, S., Brinchmann, J., White, S. D. M., & Tremonti, C. A. 2005, *MNRAS*, 362, 41
- Goodman, J., & Weare, J. 2010, *CAMCS*, 5, 65
- Gould, K. M. L., Brammer, G., Valentino, F., et al. 2023, *AJ*, 165, 248
- Goulding, A. D., Greene, J. E., Setton, D. J., et al. 2023, *ApJL*, 955, L24
- Grogin, N. A., Kocevski, D. D., Faber, S. M., et al. 2011, *ApJS*, 197, 35
- Gutkin, J., Charlot, S., & Bruzual, G. 2016, *MNRAS*, 462, 1757
- Harris, C. R., Millman, K. J., van der Walt, S. J., et al. 2020, *Natur*, 585, 357
- Hinshaw, G., Larson, D., Komatsu, E., et al. 2013, *ApJS*, 208, 19
- Hoaglin, D. C., Mosteller, F., & Tukey, J. W. 1983, *Understanding Robust and Exploratory Data Analysis* (New York: Wiley)
- Hunter, J. D. 2007, *CSE*, 9, 90
- Johnson, B. D., Leja, J., Conroy, C., & Speagle, J. S. 2021, *ApJS*, 254, 22
- Kannan, R., Springel, V., Hernquist, L., et al. 2023, *MNRAS*, 524, 2594
- Kodra, D., Andrews, B. H., Newman, J. A., et al. 2023, *ApJ*, 942, 36
- Kriek, M., Conroy, C., van Dokkum, P. G., et al. 2016, *Natur*, 540, 248
- Kroupa, P. 2001, *MNRAS*, 322, 231
- La Barbera, F., Ferreras, I., Vazdekis, A., et al. 2013, *MNRAS*, 433, 3017
- Labbé, I., Franx, M., Rudnick, G., et al. 2003, *AJ*, 125, 1107
- Labbé, I., van Dokkum, P., Nelson, E., et al. 2023, *Natur*, 616, 266
- Lagattuta, D. J., Mould, J. R., Forbes, D. A., et al. 2017, *ApJ*, 846, 166
- Leistedt, B., Alsing, J., Peiris, H., Mortlock, D., & Leja, J. 2023, *ApJS*, 264, 23
- Leitherer, C., Schaerer, D., Goldader, J. D., et al. 1999, *ApJS*, 123, 3
- Leja, J., Carnall, A. C., Johnson, B. D., Conroy, C., & Speagle, J. S. 2019a, *ApJ*, 876, 3
- Leja, J., Johnson, B. D., Conroy, C., et al. 2019b, *ApJ*, 877, 140
- Leja, J., Johnson, B. D., Conroy, C., van Dokkum, P. G., & Byler, N. 2017, *ApJ*, 837, 170
- Leja, J., Speagle, J. S., Johnson, B. D., et al. 2020, *ApJ*, 893, 111
- Leja, J., Tacchella, S., & Conroy, C. 2019c, *ApJL*, 880, L9
- Lotz, J. M., Koekemoer, A., Coe, D., et al. 2017, *ApJ*, 837, 97
- Lyubenova, M., Martín-Navarro, I., van de Ven, G., et al. 2016, *MNRAS*, 463, 3220
- Ma, X., Hopkins, P. F., Faucher-Giguère, C.-A., et al. 2016, *MNRAS*, 456, 2140
- Madau, P. 1995, *ApJ*, 441, 18
- Marchesini, D., Brammer, G., Morishita, T., et al. 2023, *ApJL*, 942, L25
- Mathews, E. P., Leja, J., Speagle, J. S., et al. 2023, *ApJ*, 954, 132
- Mauerhofer, V., & Dayal, P. 2023, *MNRAS*, 526, 2196
- McKinney, J., Finnerty, L., Casey, C. M., et al. 2023, *ApJL*, 946, L39
- Meneghetti, M., Natarajan, P., Coe, D., et al. 2017, *MNRAS*, 472, 3177
- Mirocha, J., & Furlanetto, S. R. 2023, *MNRAS*, 519, 843
- Mitchell, P. D., Lacey, C. G., Baugh, C. M., & Cole, S. 2013, *MNRAS*, 435, 87
- Naidu, R. P., Oesch, P. A., Setton, D. J., et al. 2022, arXiv:2208.02794
- Newman, J. A., & Gruen, D. 2022, *ARA&A*, 60, 363
- Noll, S., Burgarella, D., Giovannoli, E., et al. 2009, *A&A*, 507, 1793
- Onodera, M., Carollo, C. M., Renzini, A., et al. 2015, *ApJ*, 808, 161
- Pacifici, C., Iyer, K. G., Mobasher, B., et al. 2023, *ApJ*, 944, 141
- Reddy, N. A., Topping, M. W., Sanders, R. L., Shapley, A. E., & Brammer, G. 2023, *ApJ*, 952, 167
- Richard, J., Claeysens, A., Lagattuta, D., et al. 2021, *A&A*, 646, A83
- Rieke, M. J., Kelly, D. M., Misselt, K., et al. 2023, *PASP*, 135, 028001
- Rigby, J., Perrin, M., McElwain, M., et al. 2023, *PASP*, 135, 048001
- Salpeter, E. E. 1955, *ApJ*, 121, 161
- Sánchez-Blázquez, P., Peletier, R. F., Jiménez-Vicente, J., et al. 2006, *MNRAS*, 371, 703
- Schaerer, D., & de Barros, S. 2009, *A&A*, 502, 423
- Skilling, J. 2004, in *AIP Conf. Proc.* 735, *Bayesian Inference and Maximum Entropy Methods in Science and Engineering*, ed. R. Fischer, R. Preuss, & U. V. Toussaint (Melville, NY: AIP), 395
- Smit, R., Bouwens, R. J., Labbé, I., et al. 2014, *ApJ*, 784, 58
- Speagle, J. S. 2020, *MNRAS*, 493, 3132
- Spiniello, C., Trager, S., Koopmans, L. V. E., & Conroy, C. 2014, *MNRAS*, 438, 1483
- Stanway, E. R., & Eldridge, J. J. 2018, *MNRAS*, 479, 75
- Stark, D. P., Schenker, M. A., Ellis, R., et al. 2013, *ApJ*, 763, 129
- Steidel, C. C., Giallisco, M., Pettini, M., Dickinson, M., & Adelberger, K. L. 1996, *ApJL*, 462, L17
- Steidel, C. C., Strom, A. L., Pettini, M., et al. 2016, *ApJ*, 826, 159
- Steinhardt, C. L., Jauzac, M., Acebron, A., et al. 2020, *ApJS*, 247, 64
- Steinhardt, C. L., Kokorev, V., Rusakov, V., Garcia, E., & Sneppen, A. 2023, *ApJL*, 951, L40
- Strom, A. L., Steidel, C. C., Rudie, G. C., Trainor, R. F., & Pettini, M. 2018, *ApJ*, 868, 117
- Tacchella, S., Conroy, C., Faber, S. M., et al. 2022, *ApJ*, 926, 134
- Thomas, D., Maraston, C., Bender, R., & Mendes de Oliveira, C. 2005, *ApJ*, 621, 673
- Thorne, J. E., Robotham, A. S. G., Bellstedt, S., et al. 2022, *MNRAS*, 517, 6035
- Topping, M. W., Stark, D. P., Endsley, R., et al. 2022, *MNRAS*, 516, 975
- Treu, T., Roberts-Borsani, G., Bradac, M., et al. 2022, *ApJ*, 935, 110
- Treu, T., Schmidt, K. B., Brammer, G. B., et al. 2015, *ApJ*, 812, 114
- van Dokkum, P., Conroy, C., Villaume, A., Brodie, J., & Romanowsky, A. J. 2017, *ApJ*, 841, 68
- Vazdekis, A., Coelho, P., Cassisi, S., et al. 2015, *MNRAS*, 449, 1177
- Virtanen, P., Gommers, R., Oliphant, T. E., et al. 2020, *NatMe*, 17, 261
- Walcher, J., Groves, B., Budavári, T., & Dale, D. 2011, *Ap&SS*, 331, 1
- Wang, B., Fujimoto, S., Labbé, I., et al. 2023a, *ApJL*, 957, L34
- Wang, B., Leja, J., Atek, H., et al. 2023b, arXiv:2310.06781
- Wang, B., Leja, J., Bezanson, R., et al. 2023c, *ApJL*, 944, L58
- Wang, B., Leja, J., Villar, V. A., & Speagle, J. S. 2023d, *ApJL*, 952, L10
- Weaver, J. R., Cutler, S. E., Pan, R., et al. 2024, *ApJS*, 270, 7
- Webb, K., Balogh, M. L., Leja, J., et al. 2020, *MNRAS*, 498, 5317
- Whitler, L., Stark, D. P., Endsley, R., et al. 2023, *MNRAS*, 519, 5859
- Williams, R. J., Quadri, R. F., Franx, M., van Dokkum, P., & Labbé, I. 2009, *ApJ*, 691, 1879
- Yung, L. Y. A., Somerville, R. S., Finkelstein, S. L., Wilkins, S. M., & Gardner, J. P. 2024, *MNRAS*, 527, 5929
- Zavala, J. A., Buat, V., Casey, C. M., et al. 2023, *ApJL*, 943, L9
- Zitrin, A., Fabris, A., Merten, J., et al. 2015, *ApJ*, 801, 44